UNIVERSITY OF MINNESOTA

*Twin Cities Campus*

***Saint Anthony Falls Laboratory***
*Engineering, Environmental, Biological and Geophysical Fluid Dynamics*

*College of Science and Engineering*

*Mississippi River at 3rd Avenue S. E.*
*Minneapolis, MN 55414*

*Dept. Main Office: 612-624-4363*
*Fax: 612-624-4398*

**Project Title**: Virtual Wind Simulator with Advanced Control & Aeroelastic Model for Improving the Operation of Wind Farms

**Contract Number**: RD4-13 **Milestone Number**: 2 **Report Date**: 10/31/2016

**Principal Investigator**: Fotis Sotiropoulos
(631) 632-8380

**Contract Contact**: Bridget Foss
(612) 624-5571

**Congressional District**: (Corporate office) Minnesota $5^{th}$

**Congressional District**: (Project location) Minnesota $5^{th}$

## MILESTONE REPORT

**Executive Summary**: The goal for this project is to develop, demonstrate and transfer into practice an industry-leading numerical simulation model for optimization of performance, financial decision making, and operational planning of existing and newly planned wind energy plants. This project will leverage the previously completed Cycle 3 RDF project through which the first version of the Virtual Wind Simulator software (VWiS) was developed and validated. We will extend the capabilities of this first generation modeling tool to include the ability to simulate aeroelastic loading of the blades and incorporate current industry standards and advanced turbine control methods and technologies and we will demonstrate these capabilities via comparisons with data from utility-scale wind turbines and farms. The resulting VWiS+ modeling tool will thus be able to be used in practice to improve wind farm performance and reduce operational costs.

As planned, during this reporting period (monthly) activities have been carried out to address the following objectives:

1. Design and validation of the individual blade pitch control design;
2. Turbine control firmware development;
3. Development of advanced actuator type model for turbine blades;
4. Implementation of a blade aeroelasticity model in VWiS.

*Project funding provided by customers of Xcel Energy through a grant from the Renewable Development Fund.*

**Technical Progress:**

# 1 Progress 1: Robust control design for load reduction on a liberty wind turbine

## 1.1 An introduction of progress 1

The size of modern wind turbines has been increasing over the last several years in order to lift wind turbines to a higher power production level. This upscaling goes hand in hand with an increase in structural flexibility and as a consequence also increases the loads on the rotating and non-rotating parts of the turbine. These loads are caused by effects like wind shear, tower shadow, and turbulence. They can have significant impacts on the life cycle of the turbine. The demand of sophisticated control algorithms to actively and robustly mitigate these additional loads has consequently gathered an increased industrial and academic interest.

Classical variable-speed wind turbine control aims to maximize the power output in the different operating regions. Below rated speed, torque control is used to maintain the maximum power output at the maximum extractable power of the flow. Above rated wind speed, collective blade-pitch control is used to limit power production and rotary hub speed to a specified value by pitching all blades to a common angle. Additional algorithms have been developed in the last decade to mitigate different loads on the turbine. In [6], a good overview of possible load mitigation control techniques is provided. For example, filters to damp resonances on the tower bending and the drive-train shaft torsion load are proposed. Further, it is stated that active feedback control of the measured tower acceleration can help to suppress the dynamic tower fore-aft load by collective blade pitch. Modern wind turbines offer the possibility of even more advanced load reduction by means of pitching each blade individually. This individual blade-pitch control can effectively reduce the blade's out-of-plane loads. It requires, however, additional load measurements, either on the rotating or the non-rotating frame [7] and individual actuators on each blade.

Generally, a wind turbine consists of rotating parts (hub, blades, shaft) and non-rotating parts (nacelle, tower, etc.). Thus, its dynamical properties depend on the rotary hub position, which makes a wind turbine a periodic dynamic system. Standard control approaches for linear time invariant (LTI) systems are thus not directly applicable for the design of individual blade-pitch controllers. To overcome this issue, the multi-blade-coordinate (MBC) transformation was introduced to the wind energy field. The MBC transformation allows the projection of a system's rotating quantities onto non-rotating coordinates. The basic idea of this transformation can be illustrated by an observer in the fixed coordinate frame of the turbine. Instead of experiencing the three blade degrees of freedom individually, the observer experiences their summed effects. For a three bladed wind turbine, these summed effects can be described by the superposition of one symmetric degree of freedom, where all blades bend in the same direction, and two asymmetric degrees of freedom, where the bending of the individual blades is out of phase [4]. The two asymmetric out-of-plane degrees of freedom can be efficiently influenced by individual blade-pitch and are tackled in this paper. Note that due to the non-zero pitch angle of the blades, the out-of-plane degrees of freedom are a combination of edgewise and flapwise degrees of freedoms.

Most state-of-the-art individual blade-pitch controllers make use of MBC-transformed out-of-plane blade load signals and try to mitigate the two asymmetric loads. Two single-input-single-

output (SISO) proportional-integral or integral controllers are used to suppress the low frequency components of these loads. The actual blade-pitch commands are then generated by inverse MBC transformation, converting the control signals back to real blade-pitch commands.
Tools have been developed to not only transform the measured signals, but the whole periodic system into the non-rotating frame and approximate it by an LTI model [3]. Analyzing these models shows that the two asymmetric out-of-plane loads are adequately decoupled in the low frequency regime. For exactly this reason, the commonly used two-SISO-loops strategy works is adequate. As the decoupling argument only holds for low frequencies in the fixed frame, such controllers aim only at reducing the static loads in the fixed frame, that correspond to the 1P loads in the rotating frame. The term "P" refers to *per revolution* and indicates multiples of the rotational frequency of the turbine. The dominant (yaw and pitch) loads on the nacelle are located at 3P in the transformed frame. They are difficult to reduce with the classical strategy due to strong coupling effects that appear at higher frequencies.
Approximating the periodic model with an LTI model also enabled the application of sophisticated, model-based control approaches. Multivariable control designs were investigated in [7] based on a linear quadratic regulator and in [16] based on $H_\infty$-norm optimal control. Both controllers were shown to yield similar results as the classical two-SISO-loops strategy. One main aspect not addressed in these articles is the fact that multivariable control can be used to increase the controller bandwidth beyond what is possible with the classical strategy. The controller can then not only mitigate the static load, but also the 3P load in the MBC-transformed system. Thus in this paper, a multivariable control design approach and a clear and distinct tuning strategy for a controller that can mitigate both dominant blade and nacelle loads is presented. The control strategy is applied to the linearized model of the Clipper Liberty C96 research turbine operated by the University of Minnesota. The ultimate goal is to test the $H_\infty$ controller on the real turbine in the near future.

## 1.2 Multiblade coordinate transformation

The MBC transformation is used to transform quantities from the rotating frame to the non-rotating frame. For example, the three out-of-plane degrees of freedom of the individual blades can be transformed to the fixed frame, where they result in a collective degree of freedom, in which all blades move synchronously fore, and aft and two asymmetric degrees of freedom, in which the blades move asymmetrically fore and aft. Similar physical explanations can be found for the in-plane motions of the blades [4]. This paper focuses on the blades' out-of-plane degrees of freedom, as they can be effectively influenced with individual blade-pitch control.
For a better understanding of the MBC transformation, a short review is given in this section. The transformation matrix from the rotary frame to the fixed frame is defined by

$$T(\phi) = \frac{2}{3}\begin{bmatrix} 1/2 & 1/2 & 1/2 \\ \cos(\phi) & \cos(\phi+\frac{2}{3}\pi) & \cos(\phi+\frac{4}{3}\pi) \\ \sin(\phi) & \sin(\phi+\frac{2}{3}\pi) & \sin(\phi+\frac{4}{3}\pi) \end{bmatrix}, \tag{1.1}$$

where $\phi$ is the rotary position of the first blade. The out-of-plane loads $M$, measured on the three

blades, can be transformed with (1.1) to the non-rotating frame, resulting in one symmetric and two asymmetric loads [4]. The symmetric load is strongly connected to the thrust of the turbine, which is a byproduct of the moment (and power) generation. It can be effectively controlled via collective blade-pitch. Individual blade-pitch, on the other hand, can be efficiently used to mitigate the two asymmetric loads that appear as a pitch moment $M_{\cos}$ and a yaw moment $M_{\sin}$ on the nacelle in the fixed frame. Using the shorthand notation

$$V^T(\phi) = \begin{bmatrix} \cos(\phi) & \cos(\phi + \frac{2}{3}\pi) & \cos(\phi + \frac{4}{3}\pi) \\ \sin(\phi) & \sin(\phi + \frac{2}{3}\pi) & \sin(\phi + \frac{4}{3}\pi) \end{bmatrix} \tag{1.2}$$

for the last two rows of the matrix in (1.1), these cyclic moments are expressed in terms of the individual blade moments as

$$\begin{bmatrix} M_{\cos} \\ M_{\sin} \end{bmatrix} = \frac{2}{3} V^T(\phi) \begin{bmatrix} M_1 \\ M_2 \\ M_3 \end{bmatrix}. \tag{1.3}$$

The inverse of the MBC transformation is given by

$$T^{-1}(\phi) = \begin{bmatrix} 1 & \cos(\phi) & \sin(\phi) \\ 1 & \cos(\phi + \frac{2}{3}\pi) & \sin(\phi + \frac{2}{3}\pi) \\ 1 & \cos(\phi + \frac{4}{3}\pi) & \sin(\phi + \frac{4}{3}\pi) \end{bmatrix}. \tag{1.4}$$

This transformation is required for the implementation of an individual blade-pitch controller, designed in the MBC-transformed reference frame. The two cyclic control signals $\beta_{\cos}$ and $\beta_{\sin}$, generated by the controller, need to be transformed back into three blade-pitch angles using the second and third column of (1.4). This again is more conveniently expressed as

$$\begin{bmatrix} \beta_1 \\ \beta_2 \\ \beta_3 \end{bmatrix} = V(\phi) \begin{bmatrix} \beta_{\cos} \\ \beta_{\sin} \end{bmatrix}. \tag{1.5}$$

The individual blade-pitch commands $\beta_{\text{ind}}$ are added to the collective pitch command $\beta_{\text{col}}$, which is generated by the baseline control law from the rotational speed $\omega$ and its rated value $\omega_{\text{rated}}$. The complete control architecture is depicted in Fig. 1.1 including the region 3 rated generator torque command $\tau_{\text{rated}}$.

To be able to implement individual blade-pitch control, individual actuators and load sensors need to be available for each blade. On the Liberty wind turbine the load sensors are installed at the blade roots, which is accounted for in the controller design.

## 1.3 Clipper wind turbine

The wind turbine considered in this paper is the utility-scale three-bladed Clipper Liberty 2.5 MW research turbine of the EOLOS Wind Energy Research Consortium located at the UMore Park in Rosemount, MN, and shown in Fig. 1.2. It has a hub height of 80 m and a rotor diameter of 96 m. It

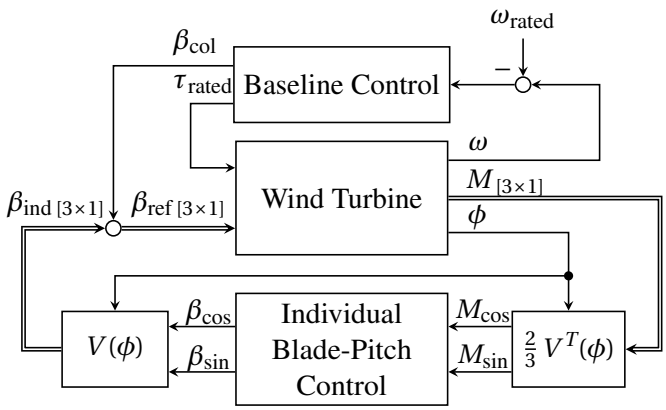


Figure 1.1: Control architecture for individual blade-pitch control.

is common to classify the operating range into standstill (region 1), variable speed (region 2), and constant speed (region 3). The turbine's cut-in wind speed is 3 m/s, from which on a $k\omega^2$ feedback is used to control the generator torque. The range from 8 to 12 m/s is used to transition between the control laws of region 2 and region 3 and is referred to as region 2.5. The rated region 3 operation starts at about 12 m/s. A scheduled proportional-integral baseline control law is used in this region to maintain rated rotor speed and moment via collective blade-pitch. The turbine cuts out at a wind speed of 25 m/s.

### 1.3.1 Nonlinear Model

An industrial high-fidelity nonlinear simulation model of the Clipper wind turbine in the Fatigue, Aerodynamics, Structures, and Turbulence (FAST) simulator [19] is used. The overall model features a detailed structural model with various degrees of freedom of the turbine and simulates steady aerodynamics. Linear first order models for actuators and sensors are included. The generator dynamics are neglected, as the power electronics on modern utility-scale wind turbines ensure a much faster torque response time than encountered in the rest of the system. The model is augmented with the certified Clipper baseline control law for the different wind regimes as described above. This baseline law includes protection functions that reduce the torque and power overshoots in region 3 in case of turbulence.

### 1.3.2 Linear Model

The FAST code provides algorithms to trim the model around a defined operating point and to derive linearized models for different rotary positions [19]. In this way, a periodic state space model in a gridded format is available. The model is of $17^{\text{th}}$ order and includes the rotary shaft velocity, four states describing the tower fore-aft and side-to-side flexibility, as well as six states to describe the first flapwise bending and six states to describe the first edgewise bending of the blades in the rotary frame.

Figure 1.2: UMN's research turbine [1].

The MBC transformation cannot only be applied to signals but also allows the conversion of a periodic state space model from a rotating into a non-rotating coordinate system. The derivation of the state transformation is not provided here due to a lack of space, but interested readers find clear derivations in [3, 27]. As for the signals, the flapwise and edgewise states are transformed to symmetric and asymmetric states, also referred to as collective and cyclic states [4]. While the MBC transformation still results in a periodic system, analyses have shown that this transformed system can be approximated well by an LTI model obtained from averaging over the rotary position [3]. Such an LTI model serves as the design model for the individual blade-pitch controller in this paper. Its inputs are the cyclic pitch commands $\beta_{\cos}$ and $\beta_{\sin}$ as defined in (1.5) and its outputs are the cyclic moments $M_{\cos}$ and $M_{\sin}$ as defined in (1.3). It can be shown that cyclic pitch commands do not influence the collective load of the turbine. This is an important fact, as the individual blade-pitch control algorithm should not change the thrust and the torque of the turbine in order to maintain the power output at its desired level.
The wind turbine model is linearized for different wind speeds along the baseline controller scheduling trajectory, defined by generator torque and blade pitch angle. Fig. 1.3 depicts the poles of the resulting LTI model in dependence on the wind speed. The pole near the origin corresponds to the rotary velocity of the turbine and nearly acts as a pure integrator. The tower's first side-to-side and fore-aft modes at around 2 rad/s show low damping but remain almost constant over the wind speed. The flapwise modes increase in frequency in the region 2 and 2.5 operation. After the rated rotation speed of the turbine is reached, the damping of these modes increases with increasing

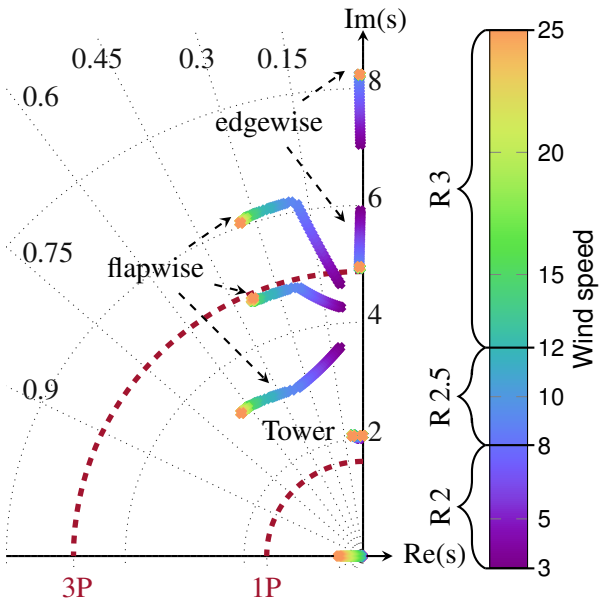


Figure 1.3: Pole migration for variation in the wind speed.

wind speed while the frequency remains unchanged. The red lines in the figure represent the 1P and 3P frequencies of the turbine in region 3. One of the flapwise modes and one of the edgewise modes can be seen to approach the 3P frequency. An overlapping of the turbine modes with these frequencies potentially causes problems, as normal operation of the turbine excites dynamics at these frequencies. The flapwise mode that approaches the 3P frequency is considered safe, as it is rather well damped. The edgewise mode, on the other hand, is likely to cause unwanted effects in region 3, due to its poor damping. The third edgewise mode is located around 13 rad/s and is not shown in the figure.

## 1.4 Multivariable control law design

The MBC-transformed and averaged Clipper model at a fixed wind speed of 12 m/s is used as the design model. This wind speed was chosen as design point as it was possible to design a controller providing closed loop stability in the whole region 3 operating region. Fig. 1.4 shows the Bode plot from cyclic blade-pitch commands to cyclic moments, normalized by the DC-gains of the diagonal elements. These cyclic moments induce yaw and pitch loads on the nacelle. Notably, the off-diagonal elements have magnitude values of around $-10$ dB in the low frequency range. For the design of classical individual blade-pitch controllers with two SISO integral control loops, this value is considered sufficiently small to neglect cross coupling, although it is far from perfect decoupling. When trying to actively mitigate the loads at higher frequencies, the coupling becomes more important with magnitudes comparable to and even above those of the diagonal elements. This observation is the main motivation for the use of multivariable control to achieve load reduction at

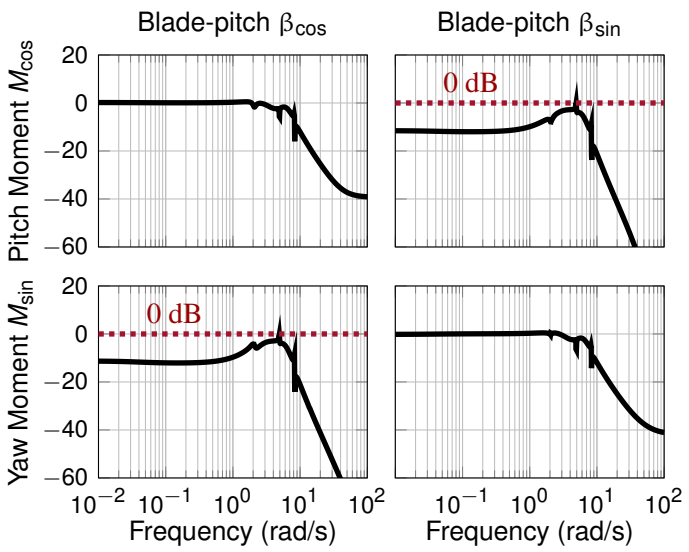


Figure 1.4: Normalized Bode magnitude plot of the 2-by-2 design system from the cyclic pitch commands to the yaw and pitch moments on the nacelle for 12 m/s wind speed.

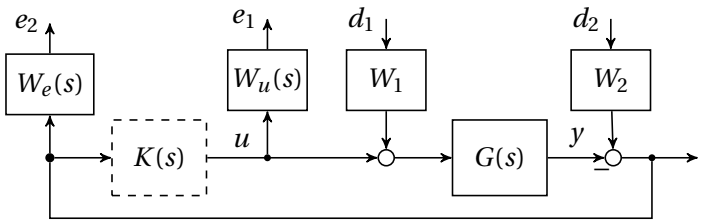


Figure 1.5: Generalized plant interconnection for the individual blade-pitch $H_\infty$ control design.

larger frequencies.

The 1P load in the rotating frame mainly translates to a constant contribution in the fixed frame. The classical two-integral-loops approach makes use of this and achieves 1P load reduction in the rotating frame by aiming at the constant load in the fixed frame. In terms of the MBC-transformed and averaged system, this can be thought of as a sensitivity reduction at zero frequency. The 2P load in the rotating frame shows up mainly as a 3P load in the fixed frame. Adapting the control strategy to also reduce these 2P loads thus involves sensitivity reduction both at zero and at the 3P frequency in the fixed frame. $H_\infty$ control is particularly useful for this task, since it allows the designer to directly "shape" the closed-loop frequency response to meet these requirements.

### 1.4.1 $H_\infty$ Control Design

The $H_\infty$-norm of an LTI system $H(s)$ from input $d$ to output $e$ is defined as

$$\|H(s)\|_\infty = \sup_\omega \bar{\sigma}(H(j\omega)) = \sup_{d \in L_2 \setminus \{0\}} \frac{\|e\|_2}{\|d\|_2}, \tag{1.6}$$

where $\bar{\sigma}(\cdot)$ denotes the largest singular value. This norm measures the maximum gain of $H(s)$, i. e., the largest amplification of $L_2$ input signals over all frequencies and input/output directions. The control problem is formulated as the closed-loop interconnection shown in Fig. 1.5 and performance is measured by the $H_\infty$-norm from $d = \left[\begin{smallmatrix} d_1 \\ d_2 \end{smallmatrix}\right]$ to $e = \left[\begin{smallmatrix} e_1 \\ e_2 \end{smallmatrix}\right]$. The corresponding transfer function is

$$\begin{bmatrix} e_1 \\ e_2 \end{bmatrix} = \begin{bmatrix} W_u & \\ & W_e \end{bmatrix} \begin{bmatrix} -T_i & K S_\mathrm{o} \\ -G S_\mathrm{i} & S_\mathrm{o} \end{bmatrix} \begin{bmatrix} W_1 & \\ & W_2 \end{bmatrix} \begin{bmatrix} d_1 \\ d_2 \end{bmatrix}. \tag{1.7}$$

In (1.7) and in the following, the dependency on the Laplace variable $s$ is not stated explicitly to shorten notation. The plant model is denoted $G$, $K$ is the controller, $S_\mathrm{o} = (I + GK)^{-1}$ is the output sensitivity function, $S_\mathrm{i} = (I + KG)^{-1}$ is the input sensitivity function, and $T_\mathrm{i} = KG(I + KG)^{-1}$ is the complementary input sensitivity function [31]. Further, $KS_\mathrm{o}$ is called control sensitivity and $GS_\mathrm{i}$ is called disturbance sensitivity. A dynamic controller $K$ that ensures stability of the closed loop and guarantees an upper bound on the $H_\infty$-norm from $d$ to $e$ can be synthesized by solving two Riccati equations [31, 17]. Synthesis algorithms that seek to minimize the upper bound are readily available, e. g., in the Matlab Robust Control Toolbox [2].

### 1.4.2 Closed Loop Shaping Strategy

The crucial part of the design is to select weights that impose a desired loop shape on the four sensitivity functions. Two cyclic loads are fed back to generate two cyclic command signals. Thus, all weightings are 2-by-2 matrices. There is, however, no apparent reason to use different weights for the individual channels and hence the matrices are selected as $W_1 = w_1 I_2$, $W_2 = w_2 I_2$, $W_e = w_e I_2$ and $W_u = w_u I_2$. Static weights $w_1$ and $w_2$ are used at the disturbance inputs.
The ratio $\frac{w_1}{w_2}$ determines the importance of rejecting input disturbances over output disturbances. For the present design, it is chosen as 10 to emphasize the importance of rejecting input disturbances. The weights are consequently selected as $w_1 = 10$ and $w_2 = 1$. The filter $w_u$ penalizes the controller output with the goal to limit control effort. Further, high frequency control action that may result in reaching the rate limits of the actuators should be avoided. Thus, $w_u$ is selected with a high gain at frequencies beyond the actuator bandwidth and a low gain for frequencies below the actuator bandwidth. For the Clipper Liberty turbine, the actuator bandwidth is 10–15 rad/s and so $w_u$ is selected with a 0 dB crossing at 6 rad/s in order to reduce control authority above this frequency. The controller is consequently forced to roll off below the actuator bandwidth. The filter $w_e$ is weights the control error, i. e. it shapes the sensitivity and disturbance sensitivity functions. A high gain of $w_e$ at a given frequency dictates a sensitivity reduction at that frequency, which results in high controller gains and improves disturbance rejection. Since the constant load in the fixed frame needs

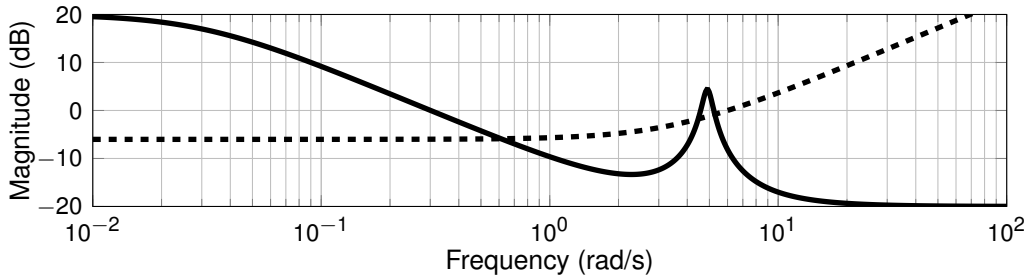


Figure 1.6: Selected filter weights $w_e$ (—) and $w_u$ (- - -).

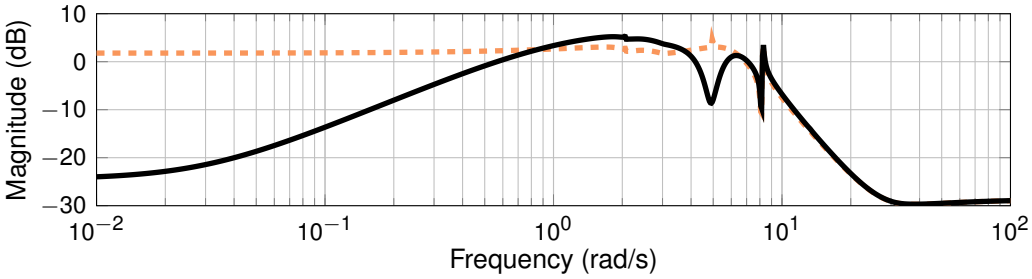


Figure 1.7: Singular value plot of the disturbance sensitivity for the open (- - -) and closed loop (—).

to be suppressed analog to the classical integral control strategy, the weight is selected to have a high gain in the low-frequency range up to 0.3 rad/s. Additionally, the controller should actively suppress the loads at the 3P frequency of about 4.8 rad/s. Thus, additional penalty is added in the vicinity of the 3P frequency by multiplying the low frequency weight with an inverse notch filter, tuned to that frequency. Fig. 1.6 shows magnitude plots of the weighting filters. Their transfer functions are

$$\begin{aligned} w_u &= 500\,\frac{s+3.464}{s+3464} \\ w_e &= 0.1\,\frac{s+3}{s+0.03}\,\frac{s^2+0.49s+24}{s^2+6.93s+24}. \end{aligned} \tag{1.8}$$

The reduction in the disturbance sensitivity is confirmed by the singular value plot depicted in Fig. 1.7. For low frequencies (<0.8 rad/s) and around the 3P (≈4.8 rad/s), the magnitude of the closed loop lies clearly below the open loop plot. As an inevitable consequence of Bode's sensitivity integral [31, 33], the sensitivity is increased between 0.8 rad/s and 4 rad/s. In the high frequency regime above roughly 5 rad/s, the open loop and closed loop are indistinguishable. This confirms the low control activity beyond that frequency.
The Bode plot of the resulting controller is depicted in Fig. 1.8. It feeds back the MBC-transformed out-of-plane blade loads $M_{\cos}$ and $M_{\sin}$ to the cyclic pitch commands $\beta_{\cos}$ and $\beta_{\sin}$. In the low-frequency range, the diagonal elements are dominant. Around the 3P frequency, the off-diagonal

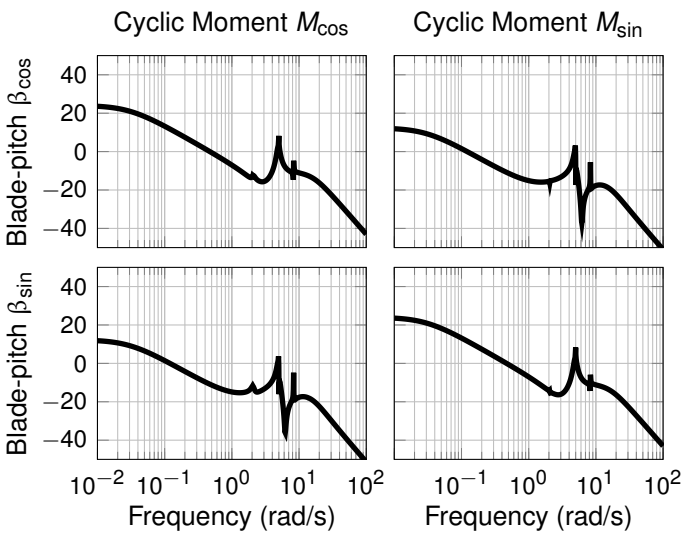


Figure 1.8: Bode magnitude plot of the controller.

elements have a comparably large magnitude. This is an important aspect of the proposed multivariable control law, as these couplings are ignored by the classical individual blade-pitch control design that consequently only works at low frequencies.

## 1.5 Verification

For the verification process of the designed controller, stability margins at the design point of 12 m/s wind speed are calculated. The dependency of these margins on the wind speed is determined in the whole operational region 3. Nonlinear simulation is used to derive damage equivalent loads and verify the load reduction capabilities of the controller.

### 1.5.1 Robustness Margins

The most common metric to quantify robustness for a control system is given by the classical gain and phase margins. The former specifies how much gain variation a single loop-transfer function can tolerate before instability occurs. The second measures the amount of phase loss that this loop can tolerate. Both margins are independent of each other. There are different specifications depending on the application field. For example, stringent certifications requirements in aerospace require at least 6 dB gain margin and 60 deg phase margin. These requirements also serve as a basis for the controller analysis in this paper. While these margins are of great practical importance, they can overlook destabilizing combinations of gain and phase that independently are considered safe. It is therefore important to also take into account simultaneous gain and phase variations. The corresponding metric is known as disk margin and can be calculated from $S_i - T_i$ and $S_o - T_o$, where $T_o$ is the output complementary sensitivity function, for the inputs and the outputs of the plant,

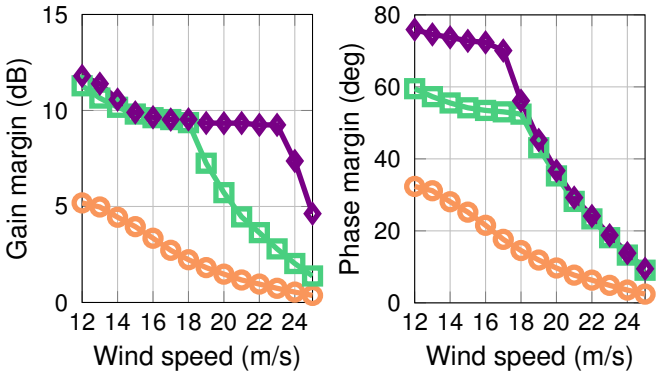


Figure 1.9: Determined classical (◆), disk (□) and multi-input multi-output (○) margins of the designed controller over wind speed.

respectively [5]. They are easily extended to the multivariable case, allowing for simultaneous perturbation of several loops. An input-output disk margin is obtained by breaking the loops at all inputs and all outputs at the same time, considering simultaneous perturbation of all signals. This is the most conservative approach to analyze the stability margins. It may seem overly conservative for the example in this paper, as the same type of load sensors and actuators are used in each of the four loops. It is, however, a valuable certificate for robustness of the system.

The resulting worst case of the classical gain and phase margins over the four SISO loops (two loops result from break points at the plant inputs, two from break points at the outputs) yields 11.8 dB and 76 deg. The worst case single-loop disk margin is 11.3 dB and 60 deg, indicating a highly robust system against single loop uncertainties. Finally, the multiple loop analysis results in a disk margin of 5.2 dB and 32 deg, which further supports the indication of high robustness. Note, a margin of above 3 dB is considered an acceptable level of degradation with respect to the single-loop margins. Encouraged by these results, the change of the margins with the change in wind speed is calculated. Wind speed variation in the operational region 3 of the Clipper turbine is rather large, lying between 12 and 25m/s.

The margins decrease when moving away from the design point but the system remains stable for all operating conditions. While until about 18 m/s, the disk margins stay in a satisfactory range, above 18 m/s a sharp decrease is observed. The worst case single-loop disk margin decreases to 1.5 dB and 10 deg, which is clearly unsatisfactory. The cause for this is revealed when looking at the critical frequency at which the worst case margins are attained. At wind speeds below 18 m/s, the critical frequency lies around 2 rad/s, while at wind speeds above 18 m/s, the critical frequency lies close to 3P. At the 3P frequency, one of the lightly damped asymmetric edgewise modes is located (see Fig. 1.3). With increased blade-pitch angle, the out-of-plane motion of the blades contains a larger contribution from the edgewise degree of freedom at higher wind speeds, where the blade-pitch angle is larger. This increasing contribution shows up as a peak in the singular value plots, which consequently decreases the margins at that frequency. It could thus be advantageous for robustness to design different controllers for different wind speeds and to use gain-scheduling or

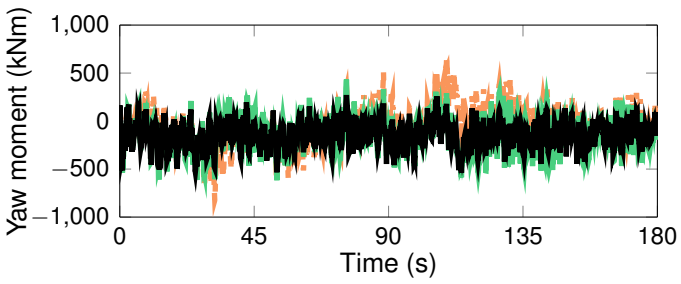


Figure 1.10: Time series of yaw bearing yaw moment for baseline (- - -), two integral loops (——), and $H_\infty$ controller (——).

linear parameter-varying control techniques in future work.

### 1.5.2 Nonlinear Simulation

The developed controller is first tested for the design wind condition at 12 m/s using the nonlinear FAST model of the Clipper turbine. A turbulence level of 7 % in all three directions is applied. The wind field has been generated using the freely available Turbsim software [18]. A state-of-practice individual blade-pitch controller is used for comparison. The controller consists of two decoupled SISO integral compensators of the form $\frac{0.001}{s}$, leading to an open loop bandwidth (0dB crossing) at around 0.25 rad/s. From the resulting simulation data, the damage equivalent loads (DELs) are calculated using the freely available software tool MCrunch [8]. The method of calculating DELs simplifies the process of producing fatigue test loads from a design load spectrum, as it can be done without specific knowledge of the blade structure or geometry. The only inputs needed are the fatigue-load spectrum and fatigue properties of the material [14]. The DELs represent a measure of equivalent fatigue damage caused by each load and take into account material properties [7]. In this work, S-N slopes of 4 and 10 are used, representative for typical steel and composite materials.
From the time series of the yaw bearing moment in Fig. 1.10, it can already be seen that the multivariable controller results in less excitations not only compared to the baseline controller, but also to the classical two-integral-loops controller.
Further insight is obtained when power spectral densities (PSD) are considered. Fig. 1.11 depicts the PSD of the blade bending moment for a wind speed of 12 m/s with a turbulence of 7 % in all three directions. The simulations results for the baseline controller without individual blade-pitch control show a high peak at the 1P frequency around 1.6 rad/s. Around the 2P frequency (4.8 rad/s), an increased loading is present, which can be seen in the lower diagram. In comparison, the classical individual blade-pitch controller that uses two integral feedback loops is able to mitigate the 1P load very well. The multivariable controller developed in this paper also achieves this reduction in the 1P load but additionally also reduces the 2P loads on the blades.
The reduction of loads at higher frequencies is confirmed when analyzing the loads that act on the non-rotating frame, namely the yaw and pitch loading on the nacelle in Fig. 1.12. The 1P blade loads appear as a constant load in the non-rotating frame, which is clearly visible in the diagrams of

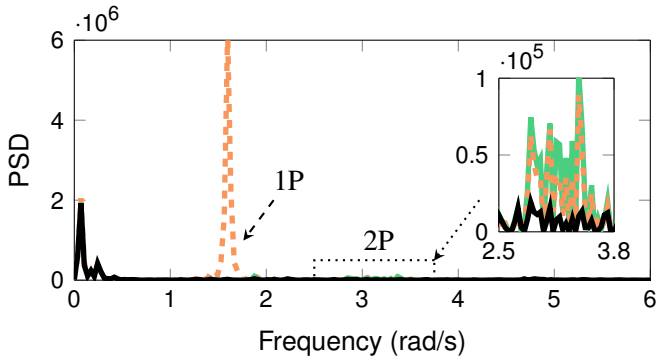


Figure 1.11: Power spectral density of the blade bending moment for baseline (- - -), two integral loops (——), and $H_\infty$ controller (——).

Fig. 1.12. Just as the 1P load on the blades, this load is mitigated well by both individual blade-pitch controllers. The 2P load on the blades produces a dominant 3P load in the fixed frame. This load is suppressed only by the multivariable controller.

Suppressing this load of course requires higher activity of the blade pitch actuation system, depicted in Fig. 1.13. For low frequencies (<0.6 rad/s), all three controllers provide the same pitch action, which is due to the dominance of the baseline control law, commanding collective pitch action. Around the 1P frequency, both individual blade-pitch controller show an increased control action in order to mitigate the constant load on the nacelle. The multivariable controller shows a large 2P control component that is required to mitigate the 2P blade loads and the 3P nacelle loads. Note that the y-axis of the plot is in log scale.

To quantify the improvements, the damage equivalent loads on the blades and the nacelle are computed. Table 1.1 presents the loads using the baseline control law alone, with classical and with $H_\infty$ individual blade-pitch control. Both, the two loop integral and the $H_\infty$ controller are able to reduce the out-of-plane bending moment on the blades. While the two integral feedback loops mainly suppress the constant load in the fixed frame, the $H_\infty$ individual blade-pitch controller works over a wider frequency range and can therefore reduce the loads even more.

The main advantage of the $H_\infty$ individual blade-pitch controller becomes clear when the pitch and yaw loads on the nacelle are considered. Due to the control activity around the 3P frequency, these loads can be reduced by about 30 %, while the classical individual blade-pitch controller lets these loads unchanged. Finally the controller is tested at higher winds speeds in region 3, namely at 16 m/s, 20 m/s and the maximum wind speed of 25 m/s. Although the robustness margins are lower as presented above, the load reduction capabilities are confirmed on these wind speeds and result in similar percentages as on the design point of 12 m/s, as depicted in Fig. 1.14. The power production is influenced below 0.8 % by the proposed individual blade-pitch controller at the tested wind speeds, confirming the decoupling of individual and collective blade-pitch control.

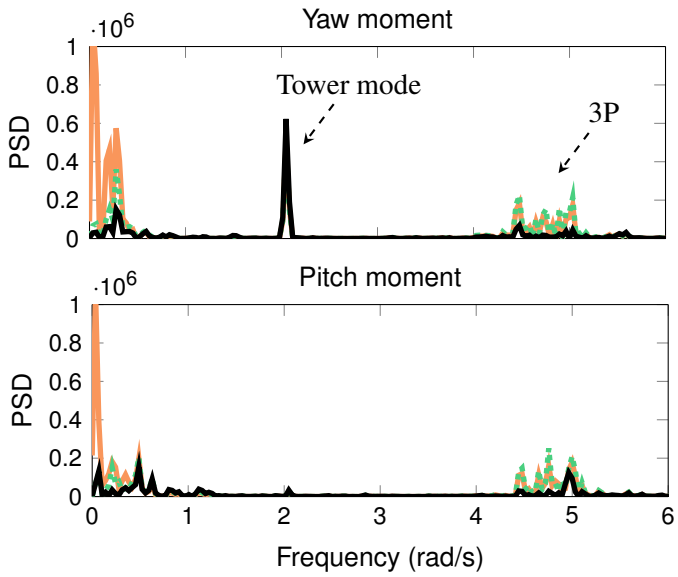


Figure 1.12: Power spectral density of the nacelle moments for baseline (- - -), two integral loops (——), and $H_\infty$ controller (——).

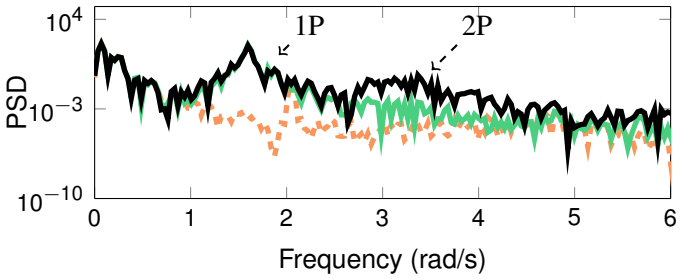


Figure 1.13: Power spectral density of commanded blade-pitch for baseline (- - -), two integral loops (——) and $H_\infty$ controller (——).

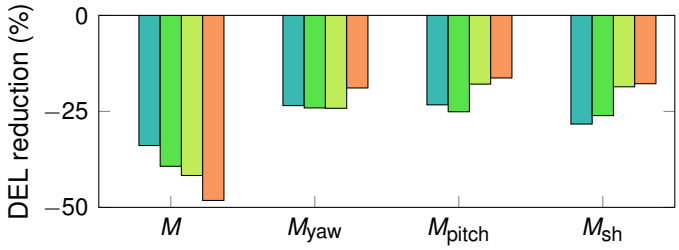


Figure 1.14: Achieved load reduction for the blade out-of-plane load $M$, the nacelle's yaw $M_{\text{yaw}}$ and pitch moment $M_{\text{pitch}}$, and the shaft bending moment around the y-axis $M_{\text{sh}}$ at 12 m/s (▭), 16 m/s (▭), 20 m/s (▭), and 25 m/s (▭).

| | Baseline | Integral | | $H_\infty$ | |
|---|---|---|---|---|---|
| **Blades** | | | | | |
| in-plane | 3196 | 3169 | -1 % | 3431 | +7 % |
| out-of-plane | 1018 | 766 | **-24 %** | 667 | **-34 %** |
| **Nacelle** | | | | | |
| yaw | 516 | 511 | -1 % | 395 | **-24 %** |
| pitch | 454 | 472 | +4 % | 347 | **-23 %** |
| **Tower** | | | | | |
| side-to-side | 4447 | 4395 | -1 % | 4776 | +7 % |
| fore-aft | 2852 | 2772 | -3 % | 2689 | -6 % |
| **Shaft** | | | | | |
| bending (y) | 480 | 501 | +5 % | 344 | **-28 %** |
| bending (z) | 487 | 483 | -1 % | 342 | **-30 %** |

Table 1.1: Damage equivalent loads (kN) based on simulation results.

### 1.5.3 Summary of progress 1

A multivariable control design approach for an individual blade-pitch control law to reduce structural loads on the rotating and non-rotating parts of a turbine has been presented. The presented approach overcomes the limitation of the classical single loops control strategy that, due to an inherent coupling at higher frequencies, can only be designed for low frequencies. The proposed procedure has been successfully applied to the to utility-scale 2.5 MW research turbine operated by the University of Minnesota. Performance and stability of the wind turbine augmented with the proposed controller was verified in industrial nonlinear high-fidelity simulations.

## 2 Progress 2: Turbine control firmware development

Accomplishments made on the turbine control firmware development are summarized as follows:

1. Completed building the code baseline upon which the project will be built, 280.13.U000.00.ă
2. Designed, implemented and tested code to support simultaneous communication with the Eolos blade sensor system and the Tcumon turbine monitor application in simulation through the Uptower HMI (UHMI) and the Downtower HMI (DHMI) ports.
3. Designed, implemented and tested code to change the UHMI port from server serial communication with Tcumon to a Modbus Master in communication with the Eolos system sending strain and temperature data through the Net32+.ă Documented and reviewed the strain and temperature
4. Modbus conversation from the Click PLC running the Eolos simulator through the Net32+ modbus-to-serial-converter and received by the TCU.

5. Designed, implemented and tested the ability to dynamically configure the Uptower HMI (UHMI) port to handle either the serial Tcumon messaging protocol or the Eolos Modbus messaging protocol.

6. Designed, implemented and tested the means to make the dynamic configuration of the UHMI port persists through power cycles.

7. Demonstrated the port assignment and strain and temperature data communication progress to the technical team.

8. Created 280.13.U000.01 control firmware to establish non-volatile memory UHMI port assignment as the first step in the two step process of creating Eolos UHMI port support.

9. 280.13.U000.01 firmware was flashed on 9/1/16 and is controlling the turbine with expected operation.

# 3 Progress 3: Actuator surface models for turbine blades and nacelle

## 3.1 An introduction of progress 3

Different rotor models, ranging from actuator disk models [9, 37, 40, 38, 25] to actuator line models [32, 11, 12, 41, 39, 34] and actuator surface models [30], have been developed in literature to parametrize the interaction between the rotor and the incoming flow without directly resolving the boundary layer flow over the blades and other structures of the rotor. In the recent paper by Kang, Yang and Sotiropoulos [22], however, it was found that the standard actuator disk and actuator line models cannot accurately capture the wake meandering caused by the interaction between the inner part and outer part of the wake for an axial-flow hydrokinetic turbine, and underpredict the turbulence intensity in the far wake. It has been shown in previous works [37, 34] that incorporating the effects of nacelle and tower in the typical actuator disk and actuator line models can improve the prediction of velocity deficit in the near wake. However, the corresponding improvement in predicting the maximum turbulence intensity in the far wake is limited as shown in [34]. The objective of this work is to develop a new class of actuator surface models for both turbine blades and nacelle incorporating more geometrical details to more accurately predict both near wake velocity deficit, and wake meandering at far wake locations.

## 3.2 Flow solver

The governing equations are the three-dimensional, unsteady, filtered continuity and Navier-Stokes equations in non-orthogonal, generalized, curvilinear coordinates, which read in compact tensor notation (repeated indices imply summation) as follows ($i, j = 1,2,3$):

$$J\frac{\partial U^i}{\partial \xi^i} = 0, \tag{3.1}$$

$$\frac{1}{J}\frac{\partial U^i}{\partial t} = \frac{\xi_l^i}{J}\left(-\frac{\partial}{\partial \xi^j}(U^j u_l) + \frac{\mu}{\rho}\frac{\partial}{\partial \xi^j}\left(\frac{g^{jk}}{J}\frac{\partial u_l}{\partial \xi^k}\right) - \frac{1}{\rho}\frac{\partial}{\partial \xi^j}(\frac{\xi_l^j p}{J}) - \frac{1}{\rho}\frac{\partial \tau_{lj}}{\partial \xi^j} + f_l\right), \tag{3.2}$$

where $x_i$ and $\xi^i$ are the Cartesian and curvilinear coordinates, respectively, $\xi_l^i = \partial \xi^i / \partial x_l$ are the transformation metrics, $J$ is the Jacobian of the geometric transformation, $u_i$ is the $i^{th}$ component of the velocity vector in Cartesian coordinates, $U^i$=$(\xi_m^i / J) u_m$ is the contravariant volume flux, $g^{jk} = \xi_l^j \xi_l^k$ are the components of the contravariant metric tensor, $\rho$ is the density, $\mu$ is the dynamic viscosity, $p$ is the pressure, $f_l (l = 1, 2, 3)$ are the body forces introduced by the wind turbines and $\tau_{ij}$ represents the anisotropic part of the subgrid scale stress tensor, which is modelled by the dynamic eddy-viscosity subgrid scale model [15]. For the discretization and solvers of the above equations, the reader is referred to [21, 41].

## 3.3 Actuator surface model

### 3.3.1 Actuator surface model for blade

In the actuator surface model for blade, the blade geometry is represented by a surface formed by the chord lines at every radial locations of the blade. The forces are calculated in the same way as in the actuator line model using the blade element approach. The relative incoming velocity $\boldsymbol{V}_{rel}$ for calculating lift and drag coefficients is computed by

$$\boldsymbol{V}_{rel}(\boldsymbol{X}_{LE}) = u_x(\boldsymbol{X}_{LE})\boldsymbol{e}_x + (u_\theta(\boldsymbol{X}_{LE}) - \Omega r)\boldsymbol{e}_\theta \tag{3.3}$$

where $\boldsymbol{X}_{LE}$ represents the leading edge coordinates of the blade, $\Omega$ is the rotational speed of the rotor, $\boldsymbol{e}_x$ and $\boldsymbol{e}_\theta$ are the unit vectors in the rotor rotating and axial flow directions, respectively. In the present model, the axial and azimuthal components of the flow velocity, i.e. $u_x$ and $u_\theta$ are computed at the leading edge (LE in Fig. 3.1) of the blade. Generally, the leading edge point LE does not coincide with any background nodes. In the present work, the smoothed discrete delta function (i.e. the smoothed four-point cosine function) proposed by Yang et al. [42] is employed to interpolate the flow velocity at the leading edge of the blade from the background grid nodes. The forces computed on each grid node of the leading edge are then uniformly distributed onto the corresponding actuator surface meshes with the same radius from the rotor center. The forces on the blade actuator surface are then distributed to the background grid nodes for the flowfield using the same discrete delta function employed in the velocity interpolation process. The stall delay model developed by Du and Selig [13] and the tip-loss correction proposed by Shen et al. [29, 28] are employed to take into account the three-dimensional effects.

### 3.3.2 Actuator surface model for nacelle

In this model, the nacelle geometry is represented by the actual surface of the nacelle with distributed forces. The force on the actuator surface is decomposed into two parts: the normal component and the tangential component. The normal component of the force is computed in a way to

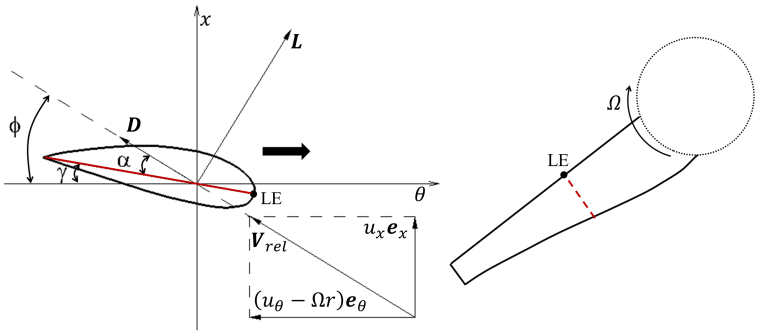


(a) A 2D airfoil element (b) Actuator surface of the blade

Figure 3.1: A schematic of the actuator surface model for turbine blade, in which the lift and drag forces calculated using the blade element approach (shown in (a)) are distributed over the actuator surface formed by the chord lines (shown in (b)).

satisfy the non-penetration condition, which is similar to the direct forcing immersed boundary methods [35, 42, 36], as follows:

$$F_n = \frac{\left(\boldsymbol{u}^d(\boldsymbol{X}) - \tilde{\boldsymbol{u}}(\boldsymbol{X})\right) \cdot \boldsymbol{n}(\boldsymbol{X})}{\Delta t}, \tag{3.4}$$

where $\boldsymbol{X}$ represents the coordinates of the nacelle surface mesh, $\boldsymbol{u}^d(\boldsymbol{X})$ is the desired velocity on the nacelle surface, $\boldsymbol{n}(\boldsymbol{X})$ is the unit vector in the normal direction of the nacelle, $\tilde{\boldsymbol{u}}$ is the velocity estimated from the previous flowfield using an explicit Euler scheme. The tangential component of the force is assumed to be proportional to the local tangential velocity and is computed as follows:

$$F_t = \frac{1}{2} C_{ASN} \left(\boldsymbol{u}^d(\boldsymbol{X}) - \tilde{\boldsymbol{u}}(\boldsymbol{X})\right) \cdot \boldsymbol{t}(\boldsymbol{X}) \left| \left(\boldsymbol{u}^d(\boldsymbol{X}) - \tilde{\boldsymbol{u}}(\boldsymbol{X})\right) \cdot \boldsymbol{t}(\boldsymbol{X}) \right|, \tag{3.5}$$

where $C_{ASN}$ is the model coefficient, and $\boldsymbol{t}$ is the tangential unit vector defined by the local tangential velocity. The smoothed discrete delta function is employed for the velocity interpolation and force distribution as in the actuator surface model for blades.

## 3.4 Test cases

Direct numerical simulation results of a sphere at $Re = UD/\nu = 3700$ (where $U$ is the incoming velocity and D is the sphere diameter) reported in [26] are employed for testing the actuator surface model for nacelle. The measurements from the “blind test" model wind turbine [23] and the hydrokinetic turbine [10] are employed to test the performance of the actuator surface models for blades and nacelle for turbine simulations. The diameter of the model wind turbine is 0.894 m with the hub of the rotor located at 0.817 m from the ground. The diameter and hub height of the hydrokinetic turbine are 0.5 m and 0.425 m, respectively. The geometry and surface meshes employed in the simulations for the two turbines are shown in Fig. 3.2. The nacelle geometry of the

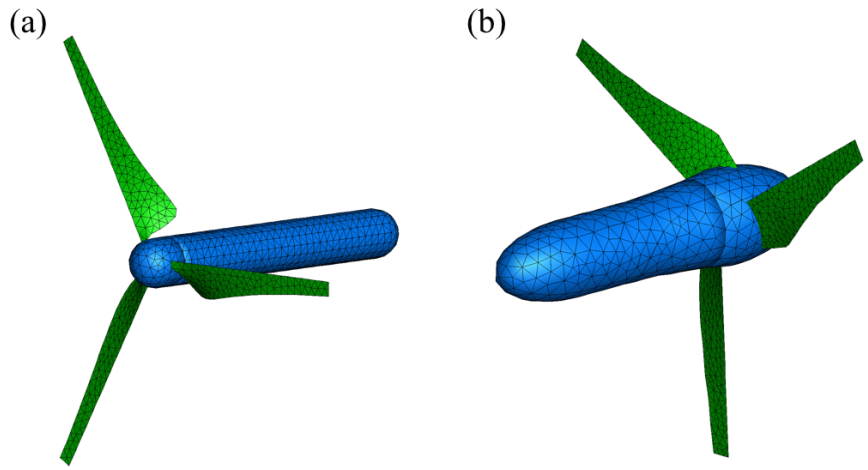


Figure 3.2: Actuator surfaces for actuator surface simulations of (a) the "blind test" model wind turbine (b) the hydrokinetic turbine. The main part of the nacelle is placed downwind of the rotor for the model turbine turbine, while upstream of the rotor for the hydrokinetic turbine.

"blind test" model wind turbine, which is not known, is represented by a hemisphere and a circular cylinder.

### 3.4.1 Flow past a sphere

This case is for testing the performance of the actuator surface model for nacelle with different values for the model coefficient $C_{ASN}$. The computational domain is $L_x \times L_y \times L_z = 19D \times 8D \times 8D$ in the streamwise direction and the two crosswise directions, respectively. The number of grid nodes is $N_x \times N_y \times N_z = 191 \times 81 \times 81$ uniformly distributed in each direction, which results the grid spacing $D/10$ everywhere. The time step is $0.02D/U$. Six cases were simulated with $C_{ASN} = 0.005, 0.05, 0.5, 1, 2$ and 4, respectively. For all the cases, the simulations were first carried out until the total kinetic energy arrived a statistically steady state, and then averaged for $tD/U = 1200$, which is equivalent to about 60 flow-throughs.

The computed drag coefficients $C_D$ for different $C_{ASN}$ are plotted in Fig. 3.3 (a). As seen, the $C_D$ for $C_{ASN} = 0.005$ and 0.05 are comparable with the DNS predictions [26] indicated by the black thick horizontal line in Fig. 3.3 (a). The $C_D$ keeps increasing when we increase the $C_{ASN}$. However, the increase is very minor when we increase $C_{ASN}$ from 2 to 4. The objective of this model is to have an acceptable prediction on the sphere wake but not the forces on the sphere. The first measure of the wake we compare for different $C_{ASN}$ is the length of the recirculation bubble as shown in Fig. 3.3 (b). It is seen that there is almost no recirculation bubble for $C_{ASN} = 0.005$ and 0.05. For higher $C_{ASN}$ (0.5, 1, 2, 4), on the other hand, the length of the circulation bubble doesn't change significantly, which is about 12% lower than the DNS predictions [26].

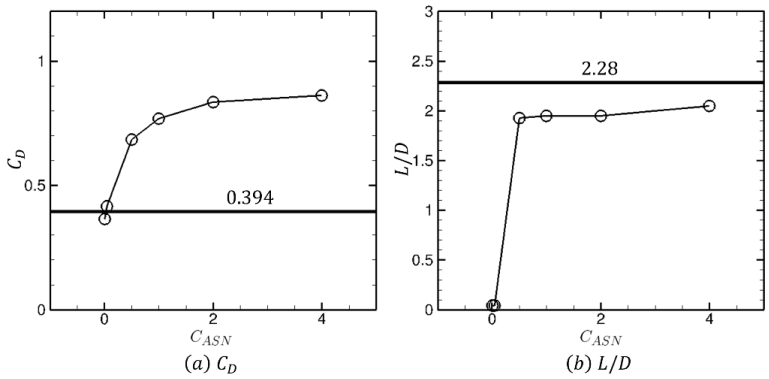


Figure 3.3: (a) Drag coefficient and (b) length of recirculation bubble for the flow past a sphere with different model coefficient $C_{ASN}$. The horizontal black thick lines indicate the DNS results from [26].

The radial profiles of the time-averaged streamwise $\langle u_x \rangle$ and radial $\langle u_r \rangle$ velocities computed from different $C_{ASN}$ are shown and compared with the DNS results [26] in Fig. 3.4. For the streamwise velocity, it is seen that velocity deficits at $x = 1.6D$, $2D$ and $3D$ in the sphere wake are greatly underpredicted for $C_{ASN} = 0.005$, which, on the other hand, are predicted very well for $C_{ASN} = 1$ and $C_{ASN} = 2$. However, the streamwise velocity deficits at $x = 5D$ and $10D$ are overpredicted for all the considered $C_{ASN}$. For the radial velocity at $x = 1.6D$ and $2D$, all the considered $C_{ASN}$ fail to predict the variations for $r/D < 0.6$, while the $C_{ASN} = 1$ and 2 predict well for $r/D > 0.6$. For further downstream locations at $x = 3D$, $5D$ and $10D$, the trends predicted by larger $C_{ASN}$ (=1 and 2) show good agreement with the DNS, which are not captured by $C_{ASN} = 0.005$, on the other hand. The model-predicted radial profiles of the streamwise and radial turbulence intensities are compared with the DNS in Fig. 3.5. At $x = 1.6D$, $2D$ and $3D$ for $r < 0.6D$, the present model with $C_{ASN} = 0.05$ underpredicts the streamwise turbulence intensity, which, on the other hand, are predicted well for $C_{ASN} = 1$ and 2. For $r > 0.6D$, however the present model with $C_{ASN} = 1$ and 2 overpredicts the streamwise turbulence intensities. This means that the model predicts a wider wake than the DNS, which can be seen more clearly from the profiles of the streamwise velocity in Fig. 3.4 (a). This makes sense because of the very coarse grid employed in the current simulations. At $x = 10D$, on the other hand, the present model with all the considered $C_{ASN}$ over-predicts the streamwise turbulence intensity. The radial turbulence intensity computed by the present model with $C_{ASN} = 0.005$ is significantly lower than the DNS predictions at $x = 1.6D$, $2D$, $3D$ and $5D$, which, however, agree well with the DNS predictions at $10D$. Overall better predictions are observed for the present model with $C_{ASN} = 1$ and 2, with the largest discrepancy happening at $x = 3D$ where the radial turbulence intensity is underpredicted significantly.

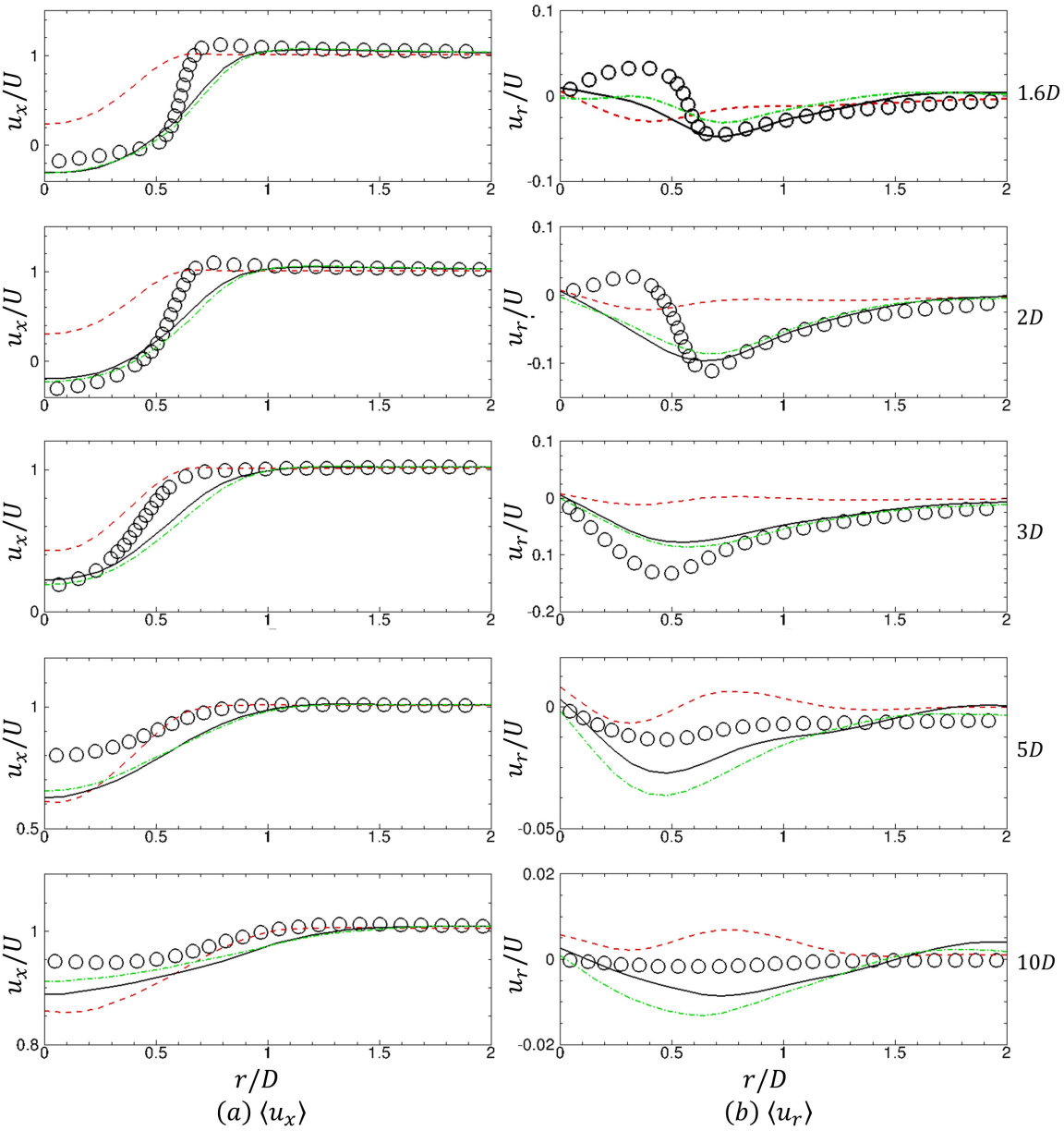


Figure 3.4: Radial profiles of time-averaged streamwise $\langle u_x \rangle$ (a) and radial $\langle u_r \rangle$ (b) velocities at different downstream locations. Symbols: the DNS results from [26]; Black solid lines: model results for $C_{ASN}$ = 1.0; Red dashed lines: model results for $C_{ASN}$ = 0.005; Green dash-dot lines: model results for $C_{ASN}$ = 2.0.

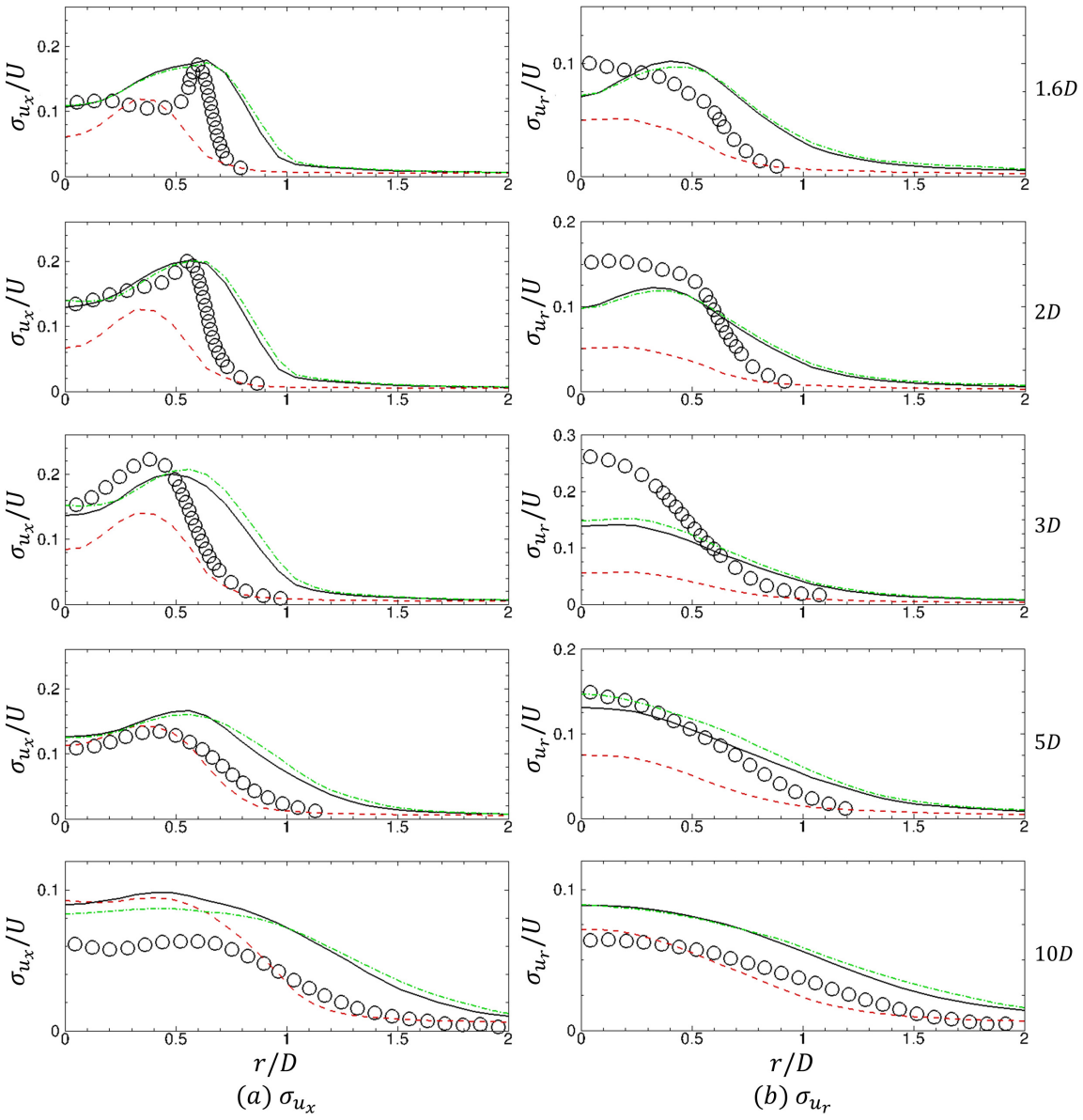


Figure 3.5: Radial profiles of streamwise $\langle u_x \rangle$ (a) and radial $\langle u_r \rangle$ (b) turbulence intensities at different downstream locations. Symbols: the DNS results from [26]; Black solid lines: model results for $C_{ASN} = 1.0$; Red dashed lines: model results for $C_{ASN} = 0.005$; Green dash-dot lines: model results for $C_{ASN} = 2.0$.

### 3.4.2 Flow over the “blind test" model wind turbine

In this section, we test the performance of the actuator surface models for simulating the “blind test" model wind turbine [23] under uniform inflow superimposed with synthetic turbulence with turbulence intensity $\sigma_{u_i}(i = 1,2,3)/U = 0.003$. The technique developed by Mann [24] is employed for generating the synthetic turbulence. The computational domain is $L_x \times L_y \times L_z = 14.5D \times 3D \times 3D$ in the streamwise, spanwise and vertical directions, respectively. The number of grid nodes is $N_x \times N_y \times N_z = 729 \times 153 \times 102$ uniformly distributed in all the three directions with grid spacing approximately $D/50$. The time step is $0.0017D/U$, where $U$=10 $ms^{-1}$ is the incoming wind speed. The Reynolds number based on the incoming wind speed and the rotor diameter is $6 \times 10^5$. In the simulations, all the cases are first carried out until the total kinetic energy reached a quasi-steady state, and subsequently the flowfields are averaged for $70T$, where $T = 2\pi/\Omega$ is the rotor revolution period. The rotational speed of the rotor is 134 $rad/s$, which gives a tip-speed ratio of 6.
The computed profiles are compared with measurements in Fig. 3.6. As seen, the actuator line model underpredicts the velocity deficit for the inner part of the wake. The actuator surface model improves the velocity deficit predictions. However, it overpredicts the velocity deficit especially in the inner part of the wake at $1D$ turbine downwind. This over prediction is possibly related to the model coefficients employed in the actuator surface simulation of the nacelle and the way how the forces on the blade interacting with the incoming flows. For the turbulence kinetic energy, both actuator surface and actuator line models underpredict the peaks near the tips of the rotor at $1D$ turbine downwind. For further downwind locations at $3D$ and $5D$, improvements on the predictions of turbulence kinetic energy are observed for the actuator surface model.

### 3.4.3 Flow over a hydrokinetic turbine

In this part, we simulate the turbulent flow over an axial-flow hydrokinetic turbine in a water tunnel using both actuator surface and actuator line models. The corresponding experiment of this case was carried out by Chamorro et al. [10] at Saint Anthony Falls Laboratory, University of Minnesota. In the work by Kang, Yang and Sotiropoulos [22], it was found that the regular actuator line model underpredicts the turbulence intensity in the far wake because it cannot capture the inner-outer wake interaction and thus the wake meandering in the far wake accurately.
In the present simulation, the computational domain is $L_x \times L_y \times L_z = 16D \times 5.5D \times 2.3D$ in the streamwise, spanwise and vertical directions, respectively, where $D$=0.5 m is the rotor dimater. The number of grid nodes is $N_x \times N_y \times N_z = 802 \times 277 \times 116$ uniformly distributed in the streamwise, spanwise and vertical directions, respectively, with grid spacing near the turbine $D/50$. The time step is $0.002D/U$, where $U$=0.4 $ms^{-1}$ is the bulk velocity. A second finer grid for testing the grid sensitivity of the actuator surface simulations is also employed with $N_x \times N_y \times N_z = 556 \times 341 \times 208$ with the grid spacing in the near wake of the turbine $D/100$ and time step $0.001D/U$. The Reynolds number based on the bulk velocity and the rotor diameter is $2 \times 10^5$. In the simulations, all the cases are first carried out until the total kinetic energy reached a quasi-steady state, and subsequently the flowfields are averaged for $90T$, where $T = 2\pi/\Omega$ is the rotor revolution period. The rotational speed of the rotor is 9.28 $rad/s$, which gives a tip-speed ratio of 5.8 based on the bulk velocity.

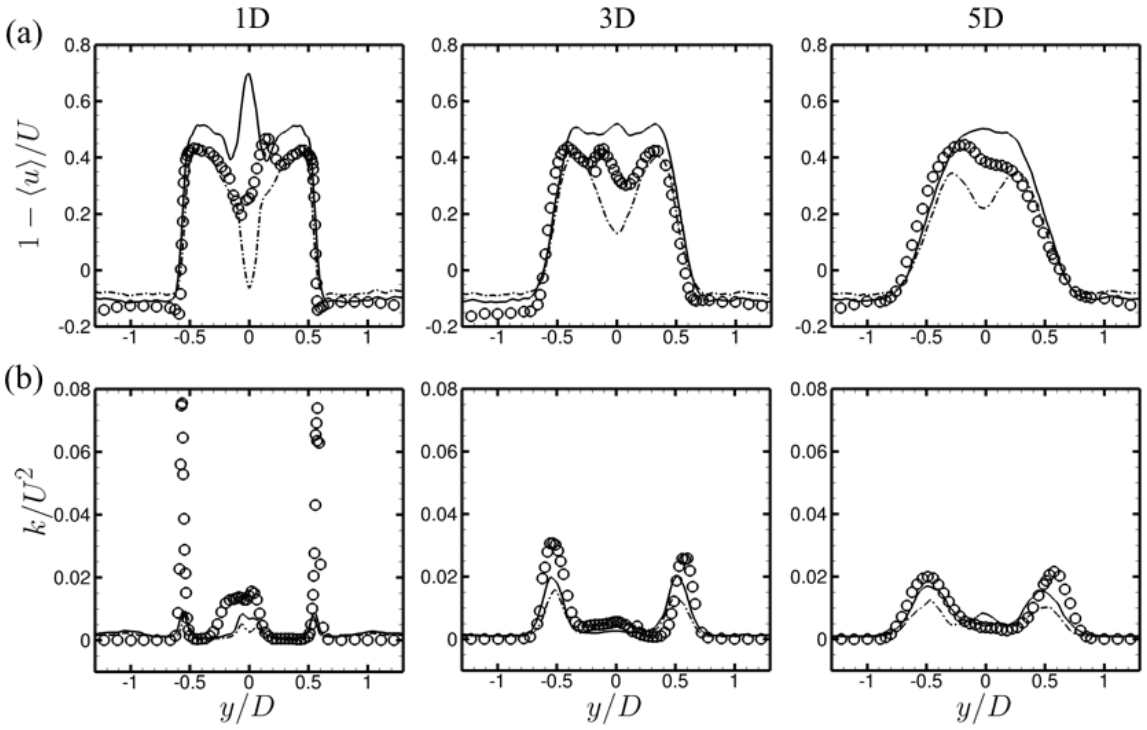


Figure 3.6: Spanwise profiles of (a) the time-averaged streamwise velocity deficit and (b) the turbulence kinetic energy at different downwind locations for the flow past the “blind test" model wind turbine. In the actuator surface simulation of nacelle, the model coefficient $C_{ASN}$ is equal to 1. Symbols: measurements from [23] ; Solid lines: actuator surface models for both blades and nacelle; Dashed lines: actuator line model for blades.

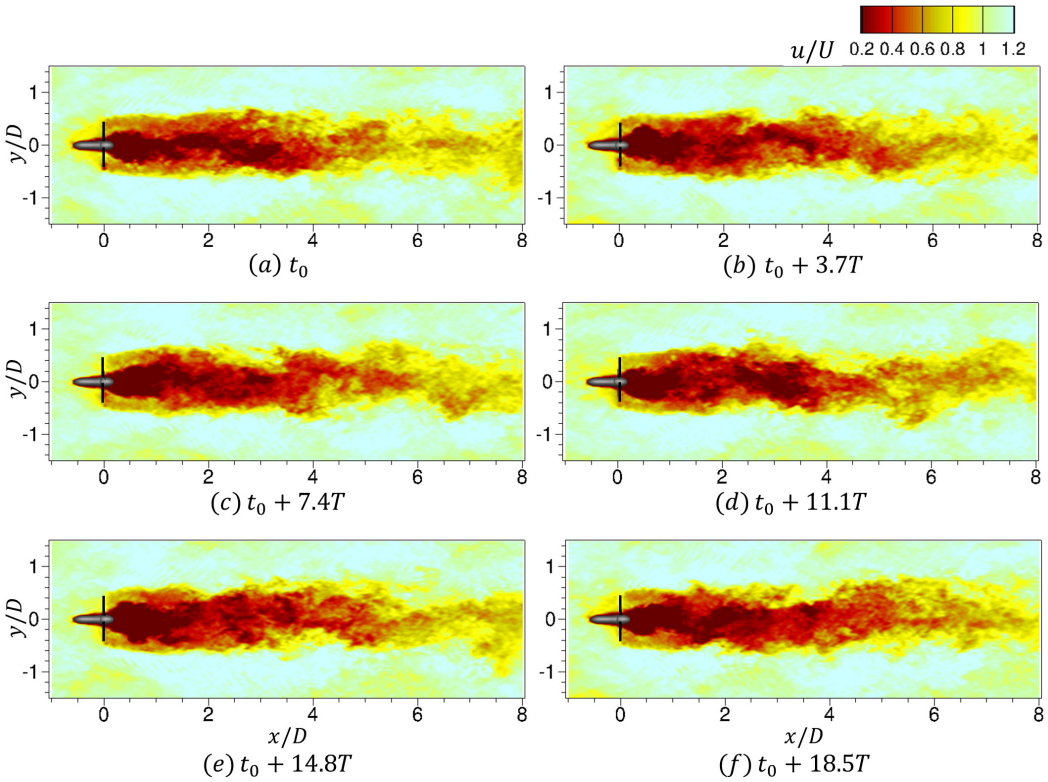


Figure 3.7: Contours of instantaneous streamwise velocity on a horizontal plane positioned at turbine hub height at different time instants, where $t_0$ and $T$ are the reference time and one rotor rotation period, respectively.

The contours of the instantaneous streamwise velocity computed from the actuator surface simulation is shown in Fig. 3.7. As seen, two features observed in the geometry-resolving simulation [22], i.e., the low-frequency motion of the inner wake near the turbine and the large-scale meandering in the far wake, are well captured by the proposed actuator surface models. Comparisons of the computed results with measurements are made in Fig. 3.8. The vertical profiles of the time-averaged streamwise velocity are shown in Fig. 3.8 (a). In this figure, we can see the wake from the nacelle is well captured by employing the actuator surface nacelle model. While the velocity deficits are somewhat overpredicted at $3D$ rotor downstream on the grid with spacing $D/100$. For the rotational velocities at $1D$ rotor downstream shown in Fig. 3.8 (b), underpredictions of their magnitudes are observed for both $D/50$ and $D/100$ grid resolutions with the actuator surface nacelle model. The prediction capability of the proposed model on the turbulence kinetic energy is demonstrated in Fig. 3.8 (c). As seen, the turbulence kinetic energy profiles computed using the actuator surface blade and nacelle models on both grid resolutions are in good agreement with the measurements at all downstream locations, which are underpredicted significantly by the actuator line model. However, the turbulence kinetic energy computed from the grid with $D/100$ is higher than that from

the grid with $D/50$. The comparison of the primary Reynolds shear stress $\langle v' w' \rangle$ profiles computed from different models is shown in Fig. 3.8 (d). One observation is that the magnitude of $\langle v' w' \rangle$ computed on the grid with spacing $D/100$ is overpredicted at 3D turbine downstream. Other than that, good agreement is obtained at further downstream locations.

### 3.5 Summary of progress 3

A new class of actuator surface models of blades and nacelle for better incorporating the geometrical effects of the blades and nacelle is proposed. The actuator surface model for nacelle was first tested by simulating the flow over a sphere at $Re = 3700$. The actuator surface models for both blade and nacelle were tested by simulating the "blind test" turbine [23] and the the axial-flow hydrokinetic turbine reported in [10, 22] with overall good agreements with measurements. It is noticed that a model coefficient $C_{ASN}$ has to be specified in the present actuator surface model for the turbine nacelle. The validity of the current employed $C_{ASN}$ value for different atmospheric regimes, such as different turbulence levels or different thermal stratifications, is not clear. Our work is being carried out to develop an actuator surface model for the nacelle without a tuning parameter.

## 4 Progress 4: Implementation of an aeroelastic model in VWiS

The aeroelastic model derived by [20] was implemented in VWiS. In this section, we will first present the aeroelastic model of [20] in Sec. 4.1 and the approach for coupling the aeroelastic model with the actuator line model in Sec. 4.2.

### 4.1 The aeroelastic model

The equations in [20] are derived by Hamilton's principle. Higher order terms are neglected in the deviation. Fig. 4.1 shows the coordinate systems employed in the model. In the inertial $(X, Y, Z)$-frame, $Y$-axis points downwind and $X, Z$-axis spans the rotor plane with $Z$-axis pointing upward. The $\hat{x}, \hat{y}, \hat{z}$-frame rotates with hub with $\hat{z}$-axis aligned with the pitch axis and $\hat{y}$-axis aligned with $Y$-axis. The angle between the two frames is denoted $\phi$ (the azimuthal angle of the rotor). The position of the blade is described in the $(x, y, z)$-frame, which is rotated $\beta$ (the pitch angle) along $\hat{z}$-axis. The elastic principle $(\eta, \xi)$-axis is centered at $(u + l_{pi}, v, w)$ in the $(x, y, z)$-frame, and rotated $\theta + \tilde{\theta}$ relative to the $(x, z)$-plane, where $u = u(s, t)$ and $v = v(s, t)$ are the deflection in the x- and y-directions, respectively, $l_{pi} = l_{pi}(s)$ is the undeformed position of elastic axis $(ea)$, $w = \int_r^s \sqrt{1 - l'^2_{pi}}\, ds - \frac{1}{2} \int_r^s \sqrt{u'^2 + v'^2 + 2l' u'}\, ds$, $\bar{\theta} = \bar{\theta}(s)$ is the pre-twist angle, and $\theta = \theta(s, t)$ is the time-dependent twist of the blade section. The independent variables $t$ and $s$ are the time and the distance from the root of the blade measured along $ea$. The $r$ is the radius of the hub, and $R$ is the radius of the rotor. The inertia of the blade is described by a concentrated mass $m = m(s)$ and a moment of rotational inertia $I_{cg} = I_{cg}(s)$ related to the center of gravity $(cg)$ for each blade section. The center of gravity is assume located on the chord $l_{cg} = l_{cg}(s)$ from $ea$. The chord is rotated $\theta + \bar{\theta}$ relative to the $(x, z)$-plane. The external forces on the blade, such as the aerodynamics forces on

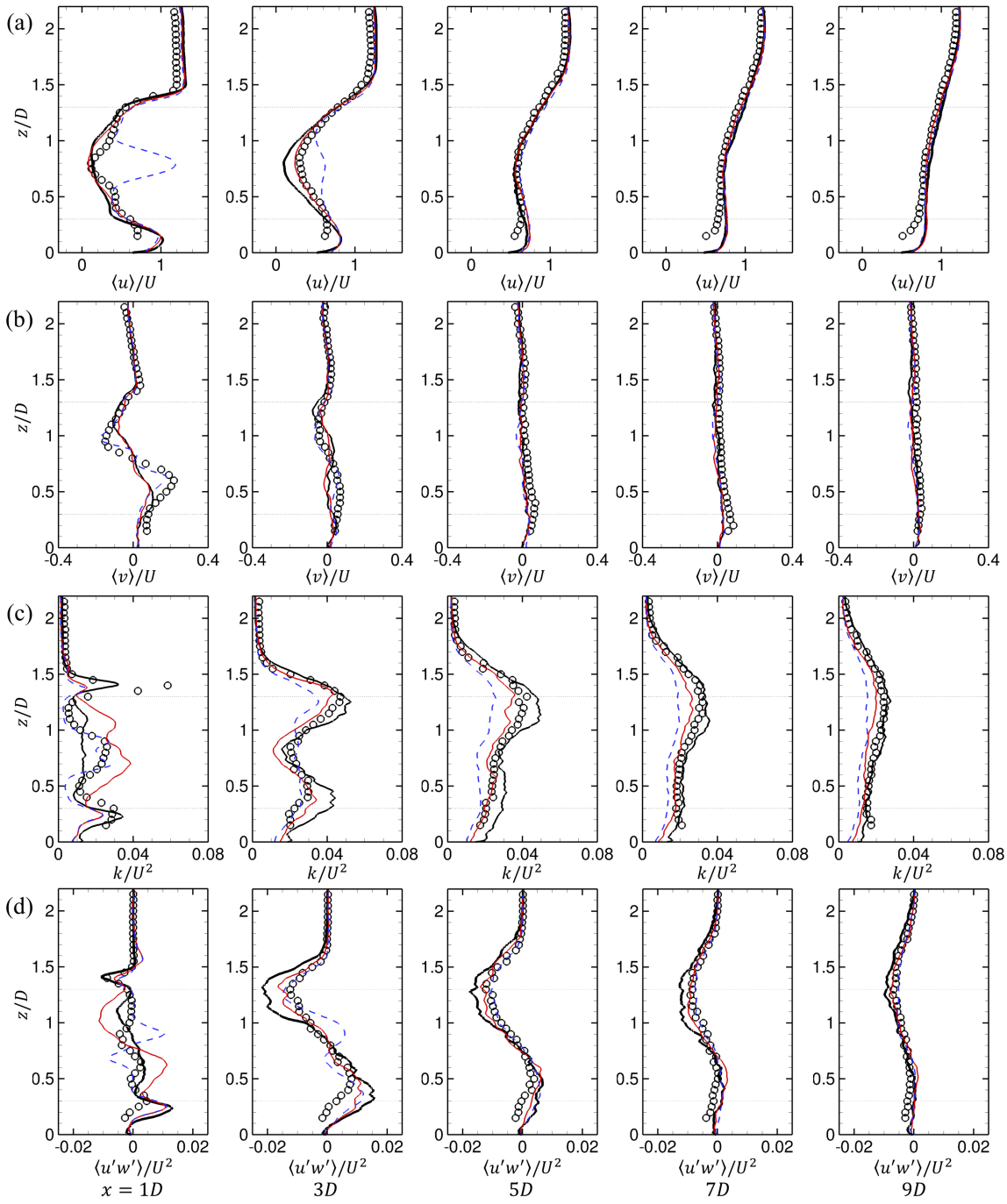


Figure 3.8: Vertical profiles of (a) the time-averaged streamwise velocity $\langle w \rangle$ and (b) the spanwise (rotational) velocities $\langle u \rangle$, (c) the turbulence kinetic energy $k$ and (d) the Reynolds shear stress $\langle v^{'} w^{'} \rangle$ at different downstream locations. Symbols: measurements from [10]; Thick black solid lines: actuator surface models for both blades and nacelle on the grid with $D/100$; Red solid lines: actuator surface models for both blades and nacelle on the grid with $D/50$; Blue dashed lines: actuator line model for blade.

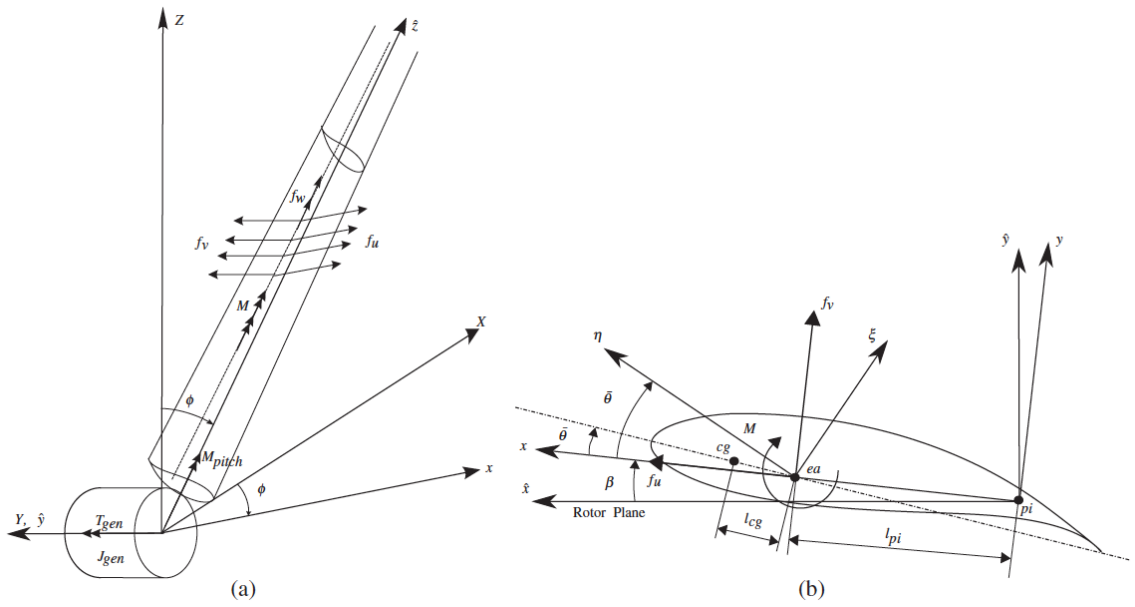


Figure 4.1: The coordinate frames in the aeroelastic model. (a) The inertial $(X, Y, Z)$-frame and the rotating $(\hat{x}, \hat{y}, \hat{z}$-frame) with $\hat{z}$-axis aligned with the pitch axis of the blade. (b) Cross section of the blade looking outward along the $\hat{z}$-axis. From [20].

the blade, are denoted by four components: $(f_u, f_v, f_w)$= $(f_u(s,t), f_v(s,t), f_w(s,t))$ in the $(x, y, z)$ directions, respectively and a twist moment $M = M(s,t)$. The forces act on the elastic axis of the blade.
The blade bending motions in the x- and y-directions are described by the following equations,

$$m\left(\ddot{u} - \ddot{\theta} l_{cg} \sin\left(\bar{\theta}\right)\right) + F_{u,1} + F_{u,2} + F_{u,3} + F_{u,4} + F_{u,5} = f_u + \left(\left(u' + l'_{pi}\right)\int_s^R f_w d\rho\right)', \tag{4.1}$$

and

$$m\left(\ddot{v} + \ddot{\theta} l_{cg} \cos\left(\bar{\theta}\right)\right) + F_{v,1} + F_{v,2} + F_{v,3} + F_{v,4} + F_{v,5} = f_v + \left(v' \int_s^R f_w d\rho\right)', \tag{4.2}$$

where $F_{u,1}$ and $F_{v,1}$ describe the influence of pitch action, $F_{u,2}$ and $F_{v,2}$ denote the influence of rotor speed, $F_{u,3}$ and $F_{v,3}$ represent the gravity effect, $F_{u,4}$ and $F_{v,4}$ are the restoring force caused by the bending stiffness of the blade, and $F_{u,5}$ and $F_{v,5}$ are for the effect of the rotor angular acceleration. The equation for the blade torsional motion is expressed as follows:

$$\left(I_{cg} + m l_{cg}^2\right)\ddot{\theta} - m l_{cg}\left(\ddot{u}\sin(\bar{\theta}) - \ddot{v}\cos(\bar{\theta})\right) + F_{\theta,1} + F_{\theta,2} + F_{\theta,3} + F_{\theta,4} + F_{\theta,5} + F_{\theta,6} = M, \tag{4.3}$$

where $F_{\theta,1}$ is from the fictitious centrifugal force, $F_{\theta,2}$ is caused by pitch action, $F_{\theta,3}$ is from the rotor acceleration, $F_{\theta,4}$ is for the effect of gravity, $F_{\theta,5}$ represents the elastic coupling between the

bending and twisting of the blade and $F_{\theta,6}$ is the restoring force caused by torsional stiffness.
The boundary conditions at the root of the blade are given by geometric constraints:

$$u(0,t) = u'(0,t) = v(0,t) = v'(0,t) = \theta(0,t) = 0. \tag{4.4}$$

The boundary conditions at the blade tip are given by

$$u''(R,t) = u'''(R,t) = v''(R,t) = v'''(R,t) = \theta'(R,t) = 0 \tag{4.5}$$

by neglecting higher-oder terms.

## 4.2 Coupling of the aeroelastic model with actuator line model

The aeroelastic model and the actuator line model are coupled through transfer of the aerodynamic forces from the flow simulation using the actuator line model to the aeroelastic model, and the blade displacements from the aeroelastic simulation to the flow simulation using the actuator line model. It is noticed that in the the convention of structure models, $u$, $v$ and $w$ represent the displacements in the $x$, $y$ and $z$ directions, respectively, which, on the other hand, represent the velocity components in the three directions in the aerodynamic simulations. In order to avoid confusion in the this section and without changing the convention in the structure model at the same time, we employ $\Delta X$, $\Delta Y$ and $\Delta Z$ for the displacements from the blade bending and twisting motions in the actuator line model equations.
In the actuator line model, the blade geometry is represented by a line in the radial direction. The lift ($\boldsymbol{L}$) and drag ($\boldsymbol{D}$) at each radial location are calculated by

$$\boldsymbol{L} = \frac{1}{2}\rho C_L c |\boldsymbol{V}_{rel}|^2 \boldsymbol{n}_L \tag{4.6}$$

and

$$\boldsymbol{D} = \frac{1}{2}\rho C_D c |\boldsymbol{V}_{rel}|^2 \boldsymbol{n}_D, \tag{4.7}$$

where $C_L$ and $C_D$ are the lift and drag coefficients, correspondingly, $c$ is the chord length, $\boldsymbol{V}_{rel}$ is the relative incoming velocity, and $\boldsymbol{n}_L$ and $\boldsymbol{n}_D$ are the unit vectors in the directions of lift and drag, respectively.
The $C_L$ and $C_D$ are functions of angle of attack. The angle of attack $\alpha$ shown in Fig. 3.1(b) has to be computed by

$$\alpha = \phi - \gamma - \theta, \tag{4.8}$$

where $\phi = -\tan^{-1}(u_x/(u_\theta - \Omega r))$, $\gamma$ is the angle including the blade twist and the blade pitch due to turbine control, $\theta$ is the angle computed from Eq. 4.3 for the blade torsional motion. The relative incoming velocity $\boldsymbol{V}_{rel}$ is computed by

$$\boldsymbol{V}_{rel} = u_x \boldsymbol{e}_x + (u_\theta - \Omega r)\boldsymbol{e}_\theta, \tag{4.9}$$

where $\Omega$ is the rotational speed of the rotor, $\boldsymbol{e}_x$ and $\boldsymbol{e}_\theta$ are the unit vectors in the axial and azimuthal

directions, respectively. Generally the grid points on the actuator surfaces do not coincide with any background nodes. We employ a smoothed discrete delta function (i.e. the smoothed four-point cosine function) proposed by Yang et al. [42] to interpolate $\boldsymbol{u}(\boldsymbol{X})$ from the values on the background grid nodes as follows:

$$\boldsymbol{u}(\boldsymbol{X}) = \sum_{\boldsymbol{x} \in g_{\boldsymbol{x}}} \boldsymbol{u}(\boldsymbol{x}) \delta_h(\boldsymbol{x} - \boldsymbol{X}) V(\boldsymbol{x}), \tag{4.10}$$

where $\boldsymbol{x}$ are the coordinates of the background grid nodes, $g_{\boldsymbol{x}}$ is the set of the background grid cells, $V = h_x h_y h_z$ ($h_x$, $h_y$, and $h_z$ are the grid spacings in the $x$, $y$ and $z$ directions, respectively) is the volume of the background grid cell, $\delta_h(\boldsymbol{x} - \boldsymbol{X}) = \frac{1}{V}\phi\left(\frac{x-X}{h_x}\right)\phi\left(\frac{y-Y}{h_y}\right)\phi\left(\frac{z-Z}{h_z}\right)$ is the discrete delta function, and $\phi$ is the smoothed four-point cosine function [42]. In the above equation, $\boldsymbol{X}$ denote the coordinates of the actuator line, which is computed as follows:

$$\boldsymbol{X} = \boldsymbol{X}_{rot} + \Delta \boldsymbol{X}_{ae} \tag{4.11}$$

Where $\boldsymbol{X}_{rot}$ are the blade coordinates determined by rotor rotation, $\Delta \boldsymbol{X}_{ae}$ are the displacements caused by blade aeroelasticity computed from Eqs. (4.1) and (4.2).
To calculate the forces on the background mesh for the flow field, the computed forces on the actuator surfaces are then distributed to the background grid nodes as follows:

$$\boldsymbol{f}(\boldsymbol{x}) = \sum_{\boldsymbol{X} \in g_{\boldsymbol{X}}} \boldsymbol{f}(\boldsymbol{X}) \delta_h(\boldsymbol{x} - \boldsymbol{X})\, A(\boldsymbol{X}), \tag{4.12}$$

where $g_{\boldsymbol{X}}$ is the set of the actuator surface grid cells and $A$ is the length of the actuator line mesh segment. The same discrete delta function as in Eq. (4.10) is employed. It is noticed that inertial frame in the actuator line flow simulation is different from that in the blade aeroelastic simulation and several coordinate systems exist in the aeroelastic simulations. Several coordinate transformations are needed in order to transfer the quantities between the two simulations.

## 4.3 Summary of progress 4

The aeroelastic model derived by [20] was implemented in VWiS. Both one-way and two-way coupled simulations can be carried out. In the one-way coupled simulation, the aerodynamic forces from the actuator line flow simulation are transferred to the blade aeroelastic simulation; while the computed aeroelastic displacements will not be considered in the actuator line simulation. This is enabled by setting $\Delta \boldsymbol{X}_{ae} = 0$ in Eq. (4.11) and $\theta = 0$ in Eq.(4.8). For the simulations when the blade displacements are smaller than the background flow mesh, this is a reasonable approach and can avoid potential numerical instability. For large turbine simulations when the aeroelastic displacements of turbine blades become significant, two-way coupled simulations are preferable. Currently, a simple loose-coupling algorithm is employed. Depending on different applications, different coupling methods will be tested and explored.

# References


[1] Eolos wind energy research consortium. www.eolos.umn.edu/facilities/eolos-wind-research-station.

[2] BALAS, G., CHIANG, R., PACKARD, A., AND SAFONOV, M. *Robust Control Toolbox User's Guide R2014b*. MathWorks.

[3] BIR, G. Multi-Blade Coordinate Transformation and its Application to Wind Turbine Analysis. In *Proc. of 46th AIAA Aerospace Sciences Meeting and Exhibit* (2008), no. 2008-1300.

[4] BIR, G., WRIGHT, A., AND BUTTERFIELD, C. Stability analysis of a variable-speed wind turbine. In *Proc. ASME Wind Energy Symposium* (1997), no. 97-0965.

[5] BLIGHT, J., DAILEY, R. L., AND GANGSAAS, D. Practical control law design for aircraft using multivariable techniques. *International Journal of Control 59*, 1 (1994), 93–137.

[6] BOSSANYI, E. Development in closed loop controller design for wind turbines. In *ASME Wind Energy Conference* (2000), pp. 64–74.

[7] BOSSANYI, E. Individual blade pitch control for load reduction. *Wind Energy 6*, 2 (2003), 119–128.

[8] BUHL, M. MCrunch UserŠs Guide for Version 1.00. Tech. Rep. NREL/TP-500-43139, National Renewable Energy Laboratory, 2008.

[9] CALAF, M., MENEVEAU, C., AND MEYERS, J. Large eddy simulation study of fully developed wind-turbine array boundary layers. *Physics of Fluids (1994-present) 22*, 1 (2010), 015110.

[10] CHAMORRO, L., HILL, C., MORTON, S., ELLIS, C., ARNDT, R., AND SOTIROPOULOS, F. On the interaction between a turbulent open channel flow and an axial-flow turbine. *Journal of Fluid Mechanics 716* (2013), 658–670.

[11] CHURCHFIELD, M. J., LEE, S., MICHALAKES, J., AND MORIARTY, P. J. A numerical study of the effects of atmospheric and wake turbulence on wind turbine dynamics. *Journal of turbulence*, 13 (2012), N14.

[12] CHURCHFIELD, M. J., LEE, S., MORIARTY, P. J., MARTINEZ, L. A., LEONARDI, S., VIJAYAKUMAR, G., AND BRASSEUR, J. G. A large-eddy simulation of wind-plant aerodynamics. *AIAA paper 537* (2012).

[13] DU, Z., AND SELIG, M. S. A 3-d stall-delay model for horizontal axis wind turbine performance prediction. *AIAA Paper 21* (1998).

[14] FREEBURY, G., AND MUSIAL, W. Determining equivalent damage loading for full-scale wind turbine blade fatigue tests. In *Proc. 19th American Society of Mechanical Engineers Wind Energy Symposium* (Reno, Nevada, USA, 2000), no. 2000-50.

[15] GERMANO, M., PIOMELLI, U., MOIN, P., AND CABOT, W. H. A dynamic subgrid-scale eddy viscosity model. *Physics of Fluids A: Fluid Dynamics (1989-1993) 3*, 7 (1991), 1760–1765.

[16] GEYLER, M., AND CASELITZ, P. Robust Multivariable Pitch Control Design for Load Reduction on Large Wind Turbines. *Journal of Solar Energy Engineering 130*, 3 (2008). 031014.

[17] GLOVER, K., AND DOYLE, J. State-space Formulae for All Stabilizing Controllers that Satisfy an $\mathscr{H}_\infty$-norm Bound and Relations to Risk Sensitivity. *Systems & Control Letters 11*, 3 (1988), 167–172.

[18] JONKMAN, B., AND KILCHER, L. TurbSim User's Guide: Version 1.50. Tech. Rep. NREL/TP-500-46198, National Renewable Energy Laboratory, 2009.

[19] JONKMAN, J. M., AND BUHL, M. L. Fast UserŠs Guide. Tech. rep., National Renewable Energy Laboratory, 2005.

[20] KALLESØE, B. S. Equations of motion for a rotor blade, including gravity, pitch action and rotor speed variations. *Wind Energy 10*, 3 (2007), 209–230.

[21] KANG, S., LIGHTBODY, A., HILL, C., AND SOTIROPOULOS, F. High-resolution numerical simulation of turbulence in natural waterways. *Advances in Water Resources 34*, 1 (2011), 98–113.

[22] KANG, S., YANG, X., AND SOTIROPOULOS, F. On the onset of wake meandering for an axial flow turbine in a turbulent open channel flow. *Journal of Fluid Mechanics 744* (2014), 376–403.

[23] KROGSTAD, P.-Å., AND ERIKSEN, P. E. Şblind testŤ calculations of the performance and wake development for a model wind turbine. *Renewable energy 50* (2013), 325–333.

[24] MANN, J. Wind field simulation. *Probabilistic engineering mechanics 13*, 4 (1998), 269–282.

[25] MIROCHA, J. D., RAJEWSKI, D. A., MARJANOVIC, N., LUNDQUIST, J. K., KOSOVIĆ, B., DRAXL, C., AND CHURCHFIELD, M. J. Investigating wind turbine impacts on near-wake flow using profiling lidar data and large-eddy simulations with an actuator disk model. *Journal of Renewable and Sustainable Energy 7*, 4 (2015), 043143.

[26] RODRIGUEZ, I., BORELL, R., LEHMKUHL, O., PEREZ SEGARRA, C. D., AND OLIVA, A. Direct numerical simulation of the flow over a sphere at re= 3700. *Journal of Fluid Mechanics 679* (2011), 263–287.

[27] SEILER, P., AND OZDEMIR, A. An optimal time-invariant approximation for wind turbine dynamics using the multi-blade coordinate transformation. In *Proc. of American Control Conference* (2013), pp. 1442–1447.

[28] SHEN, W. Z., MIKKELSEN, R., SØRENSEN, J. N., AND BAK, C. Tip loss corrections for wind turbine computations. *Wind Energy 8*, 4 (2005), 457–475.

[29] SHEN, W. Z., SØRENSEN, J. N., AND MIKKELSEN, R. Tip loss correction for actuator/navier–stokes computations. *Journal of Solar Energy Engineering 127*, 2 (2005), 209–213.

[30] SHEN, W. Z., ZHANG, J. H., AND SØRENSEN, J. N. The actuator surface model: a new navier–stokes based model for rotor computations. *Journal of Solar Energy Engineering 131*, 1 (2009), 011002.

[31] SKOGESTAD, S., AND POSTLETHWAITE, I. *Multivariable Feedback Control - Analysis and Design*. John Wiley & Sons, 2005.

[32] SÓRENSEN, J. N., AND SHEN, W. Z. Numerical modeling of wind turbine wakes. *Journal of fluids engineering 124*, 2 (2002), 393–399.

[33] STEIN, G. Respect the unstable. *IEEE Control Systems Magazine 23*, 4 (2003), 12–25.

[34] TOSSAS, L. A. M., STEVENS, R. J., AND MENEVEAU, C. Wind turbine large-eddy simulations on very coarse grid resolutions using an actuator line model. *pp. http://dx. doi. org/10.2514/6.2016–1261* (2016).

[35] UHLMANN, M. An immersed boundary method with direct forcing for the simulation of particulate flows. *Journal of Computational Physics 209*, 2 (2005), 448–476.

[36] WANG, S., AND ZHANG, X. An immersed boundary method based on discrete stream function formulation for two-and three-dimensional incompressible flows. *Journal of Computational Physics 230*, 9 (2011), 3479–3499.

[37] WU, Y.-T., AND PORTÉ-AGEL, F. Large-eddy simulation of wind-turbine wakes: evaluation of turbine parametrisations. *Boundary-layer meteorology 138*, 3 (2011), 345–366.

[38] YANG, D., MENEVEAU, C., AND SHEN, L. Large-eddy simulation of offshore wind farm. *Physics of Fluids (1994-present) 26*, 2 (2014), 025101.

[39] YANG, X., HOWARD, K. B., GUALA, M., AND SOTIROPOULOS, F. Effects of a three-dimensional hill on the wake characteristics of a model wind turbine. *Physics of Fluids (1994-present) 27*, 2 (2015), 025103.

[40] YANG, X., KANG, S., AND SOTIROPOULOS, F. Computational study and modeling of turbine spacing effects in infinite aligned wind farms. *Physics of Fluids (1994-present) 24*, 11 (2012), 115107.

[41] YANG, X., SOTIROPOULOS, F., CONZEMIUS, R. J., WACHTLER, J. N., AND STRONG, M. B. Large-eddy simulation of turbulent flow past wind turbines/farms: the virtual wind simulator (vwis). *Wind Energy* (2014).

[42] YANG, X., ZHANG, X., LI, Z., AND HE, G.-W. A smoothing technique for discrete delta functions with application to immersed boundary method in moving boundary simulations. *Journal of Computational Physics 228*, 20 (2009), 7821–7836.

**Project Status** : This project is on schedule and within budget.

## LEGAL NOTICE